國 立 交 通 大 學
光 電 工 程 研 究 所

碩士論文

利用簡單熱氣相沉積法成長之氧化銦奈米結構之相關特性研究

Research on Indium Oxide nanostructures and their characterizations grown by simple thermal vapor deposition

研究生：朱家璞

指導教授：郭浩中教授

盧廷昌教授

中華民國九十六年七月

利用簡單熱氣相沉積法成長之氧化銦奈米結構之相關特性研究

Research on Indium Oxide nanostructures and their

characterizations grown by simple thermal vapor deposition

研究生:朱家璞   Student: Chia-pu Chu

指導教授:郭浩中 教授   Advisor: Prof. Hao-chung Kuo

盧廷昌 教授   Prof. Tien-chang Lu

國 立 交 通 大 學
光 電 工 程 研 究 所
碩 士 論 文

A Thesis
Submitted to Institute of Electro-Optical Engineering
College of Electrical Engineering and Computer Science
National Chiao Tung University
in Partial Fulfillment of the Requirements
for the Degree of
Master
In

Electro-Optical Engineering

July 2007
Hsinchu, Taiwan, Republic of China

利用簡單熱氣相沉積法成長之氧化銦奈米結構之相關特性研究

研究生:朱家璞　　　　　　　　　　　指導教授:郭浩中 教授
　　　　　　　　　　　　　　　　　　　　　　　盧廷昌 教授

交通大學光電工程研究所
摘要

　　在本篇論文中，主要是探討利用熱氣相沉積方法並且推測是藉由 vapor-solid 與 vapor-liquid-solid 成長機制下所形成之氧化銦奈米結構相關特性的研究，在我的實驗中成功形成了三種奈米結構，分別為氧化氮銦奈米顆粒、氧化銦奈米串鏈、以及似水果枇杷狀的氧化銦奈米結構，在特性分析中，包含了結構與光學特性上的相關研究。結構及相關成分性的研究包含了掃描式電子顯微鏡圖像、高解析度穿透式電子顯微鏡圖像、能量散佈光譜、x 光繞射圖…，在發光特性方面，所利用的是光激發螢光光譜的分析。

　　在第一部分的氧化氮銦奈米顆粒中，奈米顆粒推測是以 VS 的成長機制形成的八面體結構，以成長溫度在攝氏 600 度至 900 度形成各個尺寸從 50 奈米至 1 微米間的奈米顆粒，並可在能量散佈光譜中，驗證此奈米結構的存在成分，並在光激發螢光光譜中，可以看出此奈米顆粒的發光範圍可以涵蓋整個紅光波段。第二部分所形成的氧化銦奈米串鏈，亦是藉由類似方式所形成，僅別於利用直徑約 20 奈米的金奈米粒子先形成長於基板表面，形成奈米串鏈與基板的嫁接，而尺寸介於 20 奈米至 100 奈米間的奈米顆粒因而相連成串鏈，並且在研究熱退火過程中，發現熱退火對於此奈米結構在光學及結構特性上皆有改善。由於欲形成奈米柱狀的氧化銦奈米結構，因此以金奈米粒子最為觸媒，而形成最後一部分的枇杷狀氧化銦奈米結構，在高解析度穿透是顯微鏡圖像中，可以看出以 VLS 成長的證據，在此部分，我分別改變通入氧氣流量及成長溫度，來研究這兩變因對於結構及發光特性上的影響，結果發現在不同成長溫度下，對於發光波段之調變，有明顯助益，波長可從 410 奈米延伸至 620 奈米。

Research on Indium Oxide nanostructures and their characterizations grown by simple thermal vapor deposition

Student: Chia-pu Chu   Advisors: Prof. Hao-chung Kuo
                                                       Prof. Tien-chang Lu

Institute of Electro-Optical Engineering, National Chiao Tung University

Abstract

In this thesis, I mainly report on the growth and the characterizations of relevant Indium Oxide nanostructures via the suggested Vapor-Solid (VS) and Vapor-Liquid-Solid (VLS) mechanism by simple thermal vapor deposition. In my experiments, I have successfully synthesized three kinds of nanostructures: they are Indium-OxyNitride nanoparticles, Indium Oxide nanochains, and loquat-like Indium Oxide nanostructures sequentially. Moreover, I have characterized the nanostructures structurally and optically. The research on the nanostrucutres' structures and the composition were carried out by Scanning Electron Microscope (SEM), High Resolution Transmission Electron Microscope (HRTEM), Energy Dispersive Spectroscopy (EDS), and X-ray Diffraction (XRD)…. On the optical emission part, I utilized Photoluminescence (PL) to investigate the emission wavelength.

In the first section of my experiments, Indium-OxyNitride nanoparticles, they are octahedrons suggested to be formed via the VS mechanism dispersed on the Silicon substrate, ranging from 50 nm to 1 um in size grown from 600 degrees to 900 degrees in Celsius. The composition is also verified by the EDS apparently. The PL shows the emission wavelength spans the whole red region. In the second section, Indium Oxide nanochains were formed in the similar way; the difference lies only in utilizing 20 nm gold nanoparticles as the catalysts and the linkers for first nanoparticle growth on the top of the Silicon substrate. And then more and more nanoparticles connected to one another sequentially by the adhesion between each other. Besides, after annealing the as-grown samples, the structural and optical quality were both improved accordingly. Owing to the objective of forming Indium nanorods or nanowires, gold nanoparticles were still introduced as the catalysts for favoring the VLS mechanism to take place. As a result, the loquat-like nanostructures were formed. And the TEM images validated the growth via the VLS mechanism. In this section, I adjusted the Oxygen flow and the growth temperature separately as factors to examine the impact on their characteristics of structure and emission wavelength. Finally, it was found the growth temperature impacted obviously on wavelength tuning. The wavelength shifted from 410 nm to 620 nm as the growth temperature increased from 500^0C to 900^0C.

Acknowledgement

Looking back for the past six years at NCTU inclusive of my undergraduate and graduate session, I am still indebted and grateful to whom I had shared the great moment with. More than that, I cherish and miss the moment to learn at class and study with my buddies. Though it was not always enjoyable in the graduate life, I reaped so much as I basked in the highly aggressive and competitive atmosphere of semiconductor laser lab. Time passes, and it comes to the terminal of my academic journey at NCTU. While I am so fortunate and blessed to be instructed by my advisors: S. C. Wang, H. C. Kuo, and T. C. Lu; I have admired the scholarly charisma, affable personality, and wholehearted endeavor out of them.

Besides, I appreciate my baseball teammate, the third baseman also my senior, Lazywind. He is such a nice guy with a good temper and care for my research work. We are just like buddies that no barricades could baffle us from working harmoniously. R. C. Gao, my optical measurement partner, is a ravishing and typical Hakka girl with a kind heart along with the extreme obedience to any task designated by our senior. I appreciate the kindness and gentleness out of her, even I feel so obliged to her help with u-PL measurement. M.J. Tsai, a partner for man˙s talk, is a very nice friend to share anything with. Despite the research field, we shared an unforgettable summer on the soccer field for watching World Cup 2006 on TV live relay. Sounds crazy, we missed almost no games. My buddies, B44 guys inclusive of TMY; I have enjoyed a wonderful year with you all. Thanks Gandpa Hua for his help on AUTOCAD drawings, Yuan˙s patience with my injured knee while playing basketball, TMY˙s motorbike and his P2P links to watch C. M. Wang˙s pitch on-line and Brother Chang˙s snacks which were always ready for me in his drawer. I am much obliged to any of my seniors, classmates, and juniors who have helped me a lot to finish the research work. Nevertheless, I have to apologize to ones I have not mentioned in the preceding.

Eventually, all I want to say is thank you GOD for paving a so fabulous and exuberant path to me. Sometimes it was challenging and thorny, however, you arranged angels beside me to help me up. I miss the teachers here, my advisors of the lab, and anyone else we have shared great memories with. From them, I learned to do good things, to do them well, and to treasure them.

Content

List of Figures

Chapter 1   Introduction and Motivation

1-6 Introduction to nanotechnology and low dimensional nanostructures

Nobel laureate Richard Feynman predicted that by the year 2000 products would be built one molecule or one atom at a time. The basic idea of nanotechnology was stated in 1959 by the famous physical scientist in the lecture "There's Plenty of Room at the Bottom." This was a truly bold vision because it would represent a new paradigm for manufacturing and constitute a fundamental economic shift analogous to a second industrial revolution. This shift is referred today as the "nanotechnology revolution," and many people consider Dr. Feynman's quote the birth of nanotechnology..

The computer industry is just one example of the advantages related to miniaturization. Getting small is a means of increasing the power and value of diverse products and services in most industries. For instance, many advances in biotechnology and the development of new drugs are the direct result of miniaturization and utilization of novel materials. The computing power, diagnostic and research power increase as tools decrease in size. Getting small allows biotechnology companies and researchers to do more complex experiments in shorter periods of time, for less money, using less material. This greatly accelerates discovery and ultimately shortens the time from concept to market for new advanced drugs and

other products. Further, nanotechnology enables companies and researchers to design

revolutionary new products using new materials and substances not accessible with

other technologies.

Nanotechnology, loosely defined as the study of functional structures with

dimensions in the 1-100 nanometer range, is emerging as a distinct and promising

field of research. Certainly, many organic chemists have designed and fabricated such

structures for decades via chemical synthesis. During the last decade, however,

developments in the areas of surface microscopy, silicon fabrication, biochemistry,

physical chemistry, and computational engineering have converged to provide

remarkable capabilities for understanding, fabricating and manipulating structures at

the atomic level.

Research in nanoscience is literally exploding, both because of the intellectual

allure of constructing matter and molecules one atom at a time, and because the new

technical capabilities permit creation of materials and devices with significant societal

impact. The rapid evolution of this new science and the opportunities for its

application promise that nanotechnology will become one of the dominant

technologies of the 21st century.

The structural goals of nanotechnology are frequently more ambitious than

making a single molecule. Often nanotechnologists wish to make arrays of identical or complex molecules, sometimes on a scale that will transcend the boundaries of the microscopic and approach the macroscopic. There are two different approaches to this end, 'top-down' and 'bottom-up.' The top-down approach is exemplified by scientists who build objects and molecular arrays using the techniques of scanning probe microscopy. The bottom-up approach is exemplified by investigators who design two- and three-dimensional chemical systems that cohere according to the rules of chemical interactions. The advantage of the top-down approach is its exquisite precision, but its disadvantage is its lack of extensive parallelism--it requires manipulating atoms and molecules practically one by one. In contrast, the bottom-up approach is massively parallel.
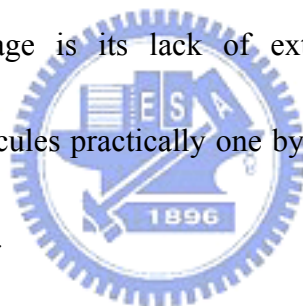
Two-dimensional (2D) nanosturctures (or quanum wells) [1] have been extensively studied by the semiconductor community because they can be conveniently prepared using techniques such as molecular beam epitaxy (MBE) [2]. Thanks to the efforts from many research groups, significant progress has also been made with respect to zero-dimensional (0D) nanostructures (or quantum dots) [3] in the past two decades. With quantum dots as a model system, a lot of intriguing chemistry and physics has been learned by studying the evolution of their fundamental properties with size [4]. Using quantum dots as active components,

various types of nanoscale devices have also been fabricated as prototypes in many research laboratories. Remarkable examples include quantum dot lasers [5], single-electron transistors [6], memory units [7], snsors[8], optical detectors [9], and light emitting diodes [10]. In recent, one-dimensional (1D) nanostructures such as nanowires, nanorods, nanobelts, and nanotubes have also become the focus of intensive research due to their unique applications in mesoscopic physics and fabrication of nanoscale devices. 1D nanostructures provide a good system to investigate the dependence of electrical and thermal transport or optical transition properties on dimensionality and size reduction also quantum confinement effect. They are also expected to play an important role as both interconnects and functional units in fabricating electronic, optoelectronic, electrochemical, and electromechanical devices with nanoscale dimensions.
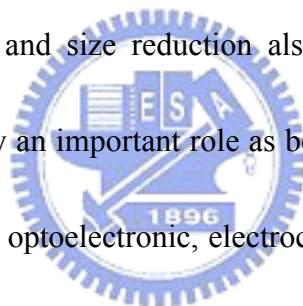
In contrast to quantum dots and wells, the advancement of 1D nanostructures have been slow until very recently, since hampered by the difficulties correlated with synthesis and fabrication of these nanostructures with well-controlled dimensions, morphology, phase purity, and chemical composition. Although 1D nanostructure can now be fabricated by using a variety of nanolithographic techniques [11], such electron-beam and focused-ion-beam writing, and x-ray or extreme-UV lithography, further development of these techniques into practical routes to a large quantities of

1D nanostructures from a diversified range of materials, swiftly, and at acceptable low costs, still requires great ingenious efforts. On the contrary, unconventional methods based on the chemical synthesis (will be discussed in the following passage) might provide an alternative and intriguing course for generating 1D nanostructures in terms of material diversity, cost, throughput, and the potential for high-volume production [12].

1-7 Methods to form low dimensional Indium Oxide nanostructures

The essence of 1D nanostructure formation is about crystallization, a process hat has been delved into for hundreds of years. The evolution of a solid from a vapor, liquid, or solid phase comprises two fundamental steps: nucleation and growth. As the concentration of the building blocks of a solid becomes sufficiently high, they aggregate into small clusters or namely, the nuclei, through homogeneous nucleation. With a continuous supply of the building, these nuclei can serve as seeds for further growth to form larger structures. Though crystallization has been studied for such a long period, very little is known quantitatively about the process. Also, it's generally accepted that the formation of a perfect crystal requires a reversible pathway between the building blocks on the solid surface and those in a fluid phases (i.e. vapor, solution, or melt). Theses conditions allow the building blocks to easily adopt correct position

in developing the long-range-ordered, crystalline lattice. Moreover, the building blocks also need to be supplied at a well-controlled rate to obtain crystals with a homogeneous composition and uniform morphology.

While developing a synthetic approach for generating nanostructures, the most significant issue to be addressed is the simultaneous control over dimensions, shapes, and the uniformity. In the past several years, multitudes of chemical methods have been reexamined or demonstrated as the "bottom-up" approach for generating 1D nanostructures with different level of control over these parameters. The following figure illustrates some of these synthetic strategies that contain 1) use of intrinsically anisotropic crystallographic structure of a solid to accomplish 1D growth (Fig. 1-2A); 2) introduction of a liquid-solid interface to reduce the symmetry of a seed (Fig. 1-2B); 3) use of various templates with 1D morphologies to direct the formation of 1D nanostructures (Fig. 1-2C); 4) use of supersaturation control to modify the growth habit of a seed; 5) use of appropriate reagents to kinetically control the growth rates of various facets of a seed (Fig. 1-2D); 6) self assembly of 0D nanostructures (Fig. 1-2E) and 7) size reduction of 1D microstructures (Fig. 1-2F).
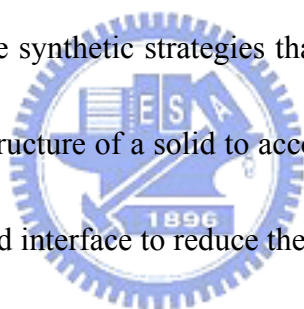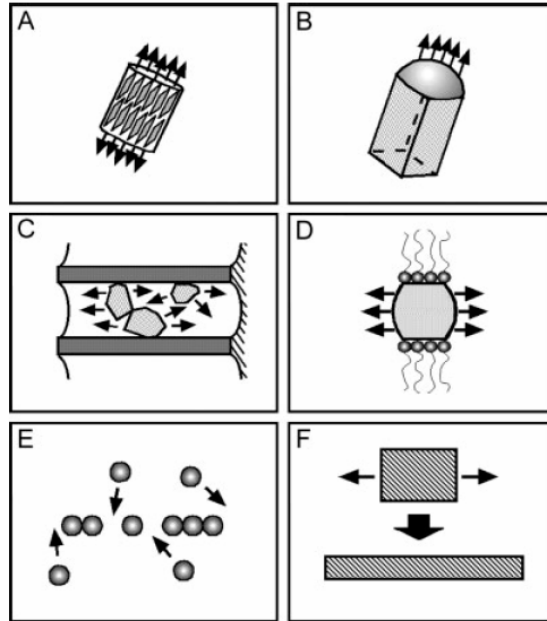
Fig. 1-2-1. Schematic illustration of six different strategies that have been demonstrated for achieving 1D growth.

The following tips are demonstrating several feasible fabrication methods for Indium Oxide 1D nanostructures. The commonly used methods of fabrication are the Chemical Vapor Deposition (CVD) and the Vapor-Liquid-Solid (VLS) methods, with other less commonly used methods as well (consisting of electrodepositing Indium onto an Alumina template, then adding oxygen, or the method of rapidly heating Indium grains in a mixture of Argon and Oxygen). How these methods work, and their usefulness are explained below.

A. Electrodeposition

This method consists of what is basically described above: An Alumina (Al_2O_3) template is fabricated by anodizing Aluminum (i.e. the Aluminum is electrically charged to about 40 V, making it the anode to a typically Platinum Cathode, in a

acidic electrolytic solution, to create the porous Alumina template of about 30 micrometers thick). After this, Indium Particles are put in the equation, dropped into the recently created Alumina template. The particles are small enough to fit into the template's pores, and are pulled in and bonded together. After this, the now formed Indium nanowires are oxidized (that is, Oxygen is added into the system), creating Indium Oxide nanowires [13, 14].
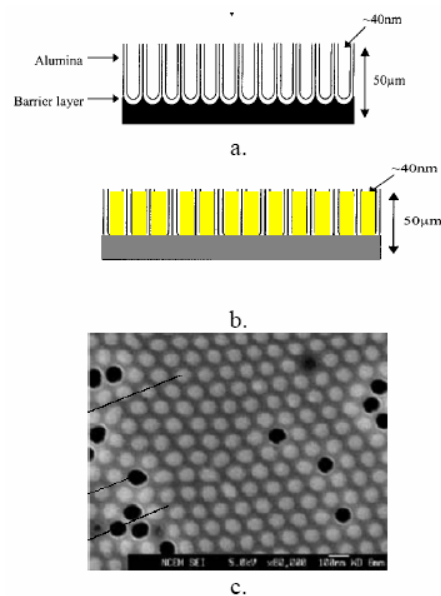
Fig. 1-2-2 (a) Cross-section of Alumina template, unfilled. (b) Alumina template, filled with newly created nanowires. (c) Top view of Alumina template, filled with newly created nanowires. Black holes refer to unfilled pores in the template white dots refer to filled pores, and the gray area in between dots is the Alumina template.

The strong points this technique makes lies in its possible high aspect ratio, along with pore size and packing density of the wires being controllable (as a function of acid strength and the amount of voltage used in the anodizing step). However, this technique can only create polycrystalline Indium Oxide nanowires, so other

techniques must be used in the fabrication of single-crystalline nanowires.

B. Rapid Heating

Through this process to create single-crystalline Indium Oxide nanowires,

Indium grains (particles) are placed in an atmosphere consisting of a mixture of

Argon and Oxygen (one such atmosphere consists of 90 % Argon and 10% Oxygen

[15]). This atmosphere is maintained at a very high temperature (about 1030ºC [15]),

and from there, using a vapor to solid approach (no catalyst is involved in this process,

unlike the CVD approach [15]), the Indium grains combine with the Oxygen in the

atmosphere and subsequently combine with other compounds as well to form the

nanowires.
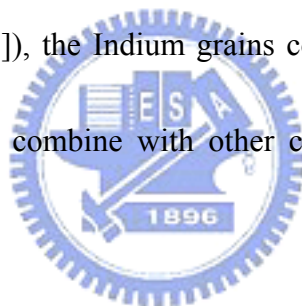
The advantage this method has is in no need for a catalyst, so further materials

do not need to be brought into the equation. However, this method is rarely used

anymore simply because of the fact that there is no way to control the diameter of the

nanowires created. Diameters can vary greatly (from 40-120 nanometers [15]), so the

need of a more controlled method is apparent, as this method is too varied for any

scientific analysis.

C. Chemical Vapor Deposition

This method is very similar to the previously explained method, but holds a few key differences. In this method, the Indium matter (which is introduced from a laser ablation process, which projects a laser onto a Indium Arsenic target, releasing Indium particles along the way due to the incident light [16]) is vaporized in a vacuum tube (similarly to the method above, as the temperature was kept at a very high temperature), then flowed into a specific containment area afterwards. After this, an Argon/Oxygen gas mixture is also flowed into this containment area. The Oxygen reacts with the Indium, creating Indium Oxide particles. Different to the method above, these molecules are then placed onto a Silicon substrate, laced with a Gold catalyst. From each Gold molecule, the nanowires grow radially outward, until the process cannot allow for more molecules on one nanowire. After all of this, the area is cooled down to allow for the solidification of the nanowires [17]..
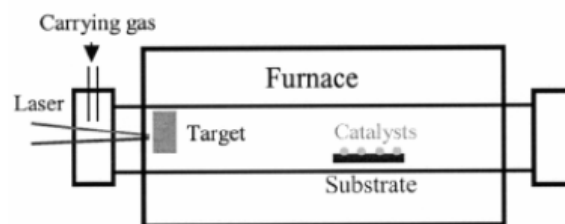
Fig. 1-2-3 Generalization of the Chemical Vapor Deposition process.

In this process, laser ablation is used to release Indium particles from the target. These particles, along with an Argon/Oxygen mixture, are flowed into a high

temperature furnace. At the opposite end of the furnace resides a Silicon substrate, with Gold atoms as catalysts. The Indium Oxide molecules, formed earlier in the furnace, is attracted to the catalysts, and forms Indium Oxide wires from it [16].

The key differences between this process and the process described above are what make CVD perform better than its rapid heating counterpart, in the sense that diameter variance is much less (typically 30-50 nanometers [16]). However, even though the variance is down, there is still very little direct control over what diameter will be produced, which makes the following process much more widely used in the fabrication of Indium Oxide nanowires.

D.   Vapor-Liquid-Solid

Vapor-Liquid-Solid (VLS) growing is a very sophisticated method, borrowing much from the Chemical Vapor Deposition process, in the fact that it uses the combination of things in vapor form to create the nanowires. Once again, Indium vapor is created using the laser ablation process on the Indium Arsenic target, which is introduced into the high temperature furnace (although there is no Oxygen present yet). However, this is where things get a bit different. Now, a Gold cluster is placed in the system, and is continually bombarded with the Indium vapor. From this continual feeding of the vapor, the Gold cluster forms into a Gold/Indium liquid drop (as the

temperature is high enough to vaporize Indium but not high enough to vaporize the combination of the two, just liquefying them), then the drop reaches supersaturation from all of the Indium, making the Indium particles grow out into a nanowire. After the Indium nanowire is created, Oxygen is then introduced, creating the single-crystalline Indium Oxide nanowire [13].
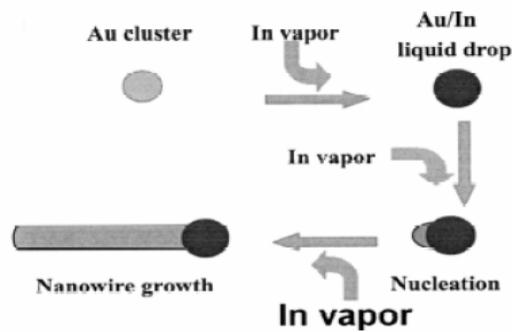
Fig. 1-2-4 Generalization of the Vapor-Liquid-Solid process.

As Indium vapor is continually supplied to the Gold cluster, the cluster forms a combination with the Indium, followed by the overabundance of Indium forming in a nanowire growth. Oxygen is then supplied to create the single-crystalline Indium Oxide nanowire.

From this process, nanowire diameter is directly controllable, as it is proportional to the size of the Gold cluster put in the system, and is basically equal to the diameter of the Gold/Indium combination. Therefore, creating consistent nanowires is now attainable, and as such, this is the most widely used method, especially when doing analysis on the properties an Indium Oxide nanowire contains [13].

1-8 Properties of Indium Oxide and Indium Oxide compound semiconductors

As far as the elements themselves go, Indium (element number 49 on the periodic table) is a fairly abundant metal, white and silvery in color, and produces a high-pitched sound when bent. A major application of Indium is to make low melting point alloys. Also notable is that Indium is a byproduct of the formation of Lead and Zinc, and many isolation processes (such as the electrolysis of Indium salts in water) are required to make Indium samples pure enough for electronic purposes [18]. Finally, plating applications exist for Indium due to its high resistance to corrosion, as well as it being used for doping semiconductors in transistor fabrication [19]. Oxygen (element number 8 on the periodic table) is a very abundant gas (which is colorless, but pale blue in a liquid state) that most life on the planet needs to live. About one fifth of the earth's atmosphere is comprised of Oxygen, and Oxygen is well known to be a highly reactive element, and forms many compounds with other elements Finally, the combination of the two, Indium Oxide (In_2O_3), the compound of interest in the fabrication of Indium Oxide Nanowires, is a crystalline yellow solid, with a very high melting point (approximately 1913°C) and also known to be fairly dense as well (approximately 7180 kg/m³) [18]. Because of these properties, it is well suited to be used for electrical and optical applications (as it is an n-type semiconductor, but also can pass over 90% of visible light through it [20]). In addition, it's a wide bandgap

material with the bandgap of around 3.5~3.6 Ev (340 nm). When it comes to such a

wide bandgap material, it may intrigue people for its application on UV LEDs' and

white illumination.

1-9 Review of thus far achievement in applications of Indium Oxide nanostructures

A. Transistor Applications

Because of the Indium Oxide nanowire's semiconductor nature, it is well suited

for use in field effect transistor applications. At the University of Southern California,

testing was conducted using 10-nanometer diameter Indium oxide nanowire as a

bridge between two metal electrodes (indicating the source and drain) over a Silicon

substrate (creating a FET with a 3 micrometer channel) [13]. Results of such testing

can be seen below:
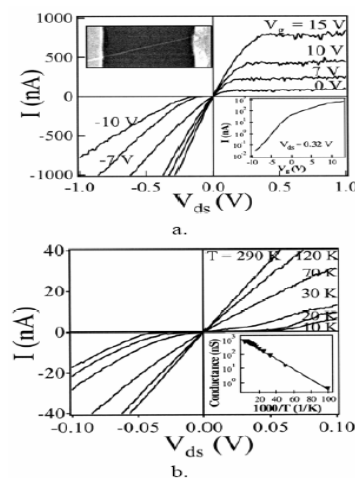
Fig. 1-4-1 (a) Current/Drain Voltage comparison graph at various gate voltages and
room temperature. (b) Current/Drain Voltage comparison at a constant gate voltage (0

V) and varying temperatures.

From the figures above, one can see that the Indium Oxide nanowire functions well as a gate for a field effect transistor application, as the output graphs are very similar to that of a regular metal oxide semiconductor field effect transistor (Mainly because the Indium Oxide nanowire is a metal oxide semiconductor) [13].

B. Chemical Sensor Applications

The ability for Indium Oxide nanowires to detect certain things at room temperature, such as chemical compounds, has turned up in recent days as well, especially for detecting the gas with high electron-affinity. Because when exposing the Indium Oxide nanowires to such the atmosphere, the electrons flowing near the surface of nanowires could be easily captures by the gas and effect would also be observed from the I-V measurement due to the slump of conductivity. From the same research team at the University of Southern California, the nanowire transistors created for the above application turned up again in this application. The transistors were placed in a vacuum area (to avoid impurities coming in), and the nanowire's conductance was monitored as a chemical compound (in this case, NO_2 or NH_3) was diluted in Argon (an inert gas so it would not react with anything) or dry air and flowed in to the vacuumed chamber. Such a test produced these results for NO_2:
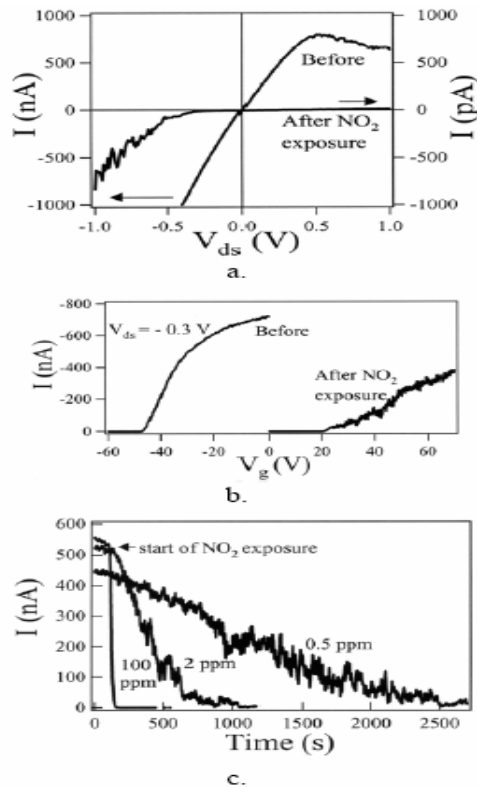
Fig. 1-4-2 (a) Current vs. Drain Voltage comparison with no gate voltage applied. The arrows indicate different scales - the before trend uses the left scale, and the after trend uses the right scale. (b) Current vs. Gate Voltage comparison with -.3 V applied to the drain. (c) Time response of the Indium Oxide nanowire under various concentrations of NO_2.

But what do these graphs say about the nanowire? In the first graph, before exposure to the compound, the trend exhibits that of a regular FET, with the well-defined linear and saturation regions. However, after the nanowire is exposed to the chemical compound, the conductance decreases dramatically, somewhere in the range of six orders of magnitude. If using such a difference in conductance as a basis, one could easily determine whether the compound was present or not. In the second graph, the chemical sensing properties of the Indium Oxide nanowire are reaffirmed, as well as other findings. As can be seen above, after exposure to the compound,

- 16 -

nanowire conductance is dramatically decreased. However, other findings pop up as well. For one, it is confirmed that the nanowire is an n-type semiconductor, as when the gate voltage negatively increased, the current drops, indicating a reduced conductance as well. Also, very important to note is the point where each of the curves flatten out, which more or less indicates the threshold point of the FET. As the compound is exposed, the threshold point increases from approximately –45 V to near +20 V, a very noticeable increase. In the final graph, one can note that the nanowire FET can detect even small concentrations of the compound; however the penalty the smaller compound gives is in the form of a much greater amount of time for the conductance to drop. From these experiments, the lowest concentration this FET was able to detect was 5 ppb. But why does the Indium Oxide nanowire act like this? This comes from NO_2 being an oxidizing gas (from it containing Oxygen in its compound). From this, the Indium Oxide readily adsorbs the molecules also captures the electrons near the nanowire's surface, which will then leave less room for free electrons logically, since there is less room for free electrons to maneuver, the conductivity decreases [13].

From these proceedings, one can use the outputs after exposure to determine how much of a compound is present in the atmosphere (from looking at reaction time), what kind of compound, or compounds, exist (from shift in threshold point or drop in

conductance), and subsequently be able to thoroughly analyze your surroundings, knowing exactly what is around you. Compared to other sensors of the same nature, it is found that the sensitivity of the nanowire is much greater, as the difference of several orders of magnitude is better than the conventional sensor's one or two orders of magnitude at the most [13].

C. Applied to Transparent Conductive Oxide

The followings are the items using Transparent Conductive Oxieds.

· Touch panels

· Electrochromic, electroluminescent and LCD displays

· Plasma displays

· Field emission displays

· Heat reflective coatings

· Energy efficient windows

· Gas sensors

· Photovoltaics

Transparent conducting oxides (TCO) thin films are widely used in applications such as the transparent electrodes of flat panel displays, solar cells and touch panels. A combination of the p and n types TCO to form a p-n junction can result in qualities ideal for optoelectronics. Some transparent oxides such as ZnO are also known to be

candidates for diluted magnetic semiconductors, and have potential for applications in spintronic devices.

A number of materials such as tin-doped indium oxide (ITO), ZnO, and SnO2 are used in many optoelectronic devices. ITO is currently the most widely used TCO. However, as indium is a relatively scarce element, the cost for ITO production is high. The other drawback of ITO films is the lack of chemical stability. The indium of an ITO layer can diffuse into the organic materials, leading to the degradation of light emitting diode (LED). Tin doped indium oxide (In_2O_3) is a transparent conducting material that is usually used in thin coating form. As a coating it is commonly deposited by methods such as electron beam evaporation or a range of sputtering techniques. The optical and electronic properties if ITO films are dependent on factors such as deposition parameters and starting materials. For instance, the film must contain a high density of charge carriers to conduct, however, the higher the density of charge carriers, the lower the transparency.

At present almost all TCO thin films are n-type semiconductors as it is extremely difficult to fabricate a p-type TCO semiconductor. However, it is crucial to fabricate the p-type in order to make active circuit components such as diodes in transparent circuits.

1-10 Motivation for my study on the growth and characterizations of Indium Oxide nanostructures

Because there are scarcely mention of the optical properties of Indium nanostructures with profound investigation and the direct utilization of such of the wide bandgap compound semiconductors, I am determined to be engrossed in the nanostructures growth along with their structural and optical characterization.

Indium oxide (In$_2$O$_3$) is a very important compound semiconductor with a large band gap around 3.5 eV and has recently attracted much attention as a material for transparent electrodes in electronic devices such as liquid crystal displays [21], solar cells [22], sensing material [23] and nanowire technology [24]. In recent, the interest in the fabrication of In$_2$O$_3$ nanostructure has been mounting because of their possibility to applications for both nanoelectronic and optoelectronic devices and the passion to deal with unclear physical properties. Wang *et al.* obtained In$_2$O$_3$ nanobelts by evaporation of In$_2$O$_3$ powders [25]. Li *et al.* grew In$_2$O$_3$ nanowires by a thermal evaporation oxidation method with a catalyst by laser ablation [16]. Piqueras *et al.* grew In$_2$O$_3$ nanoarrows in thermally treated indium nitride for different annealing time [27]. Lao *et al.* observed nanochains and nanowire networks grown by a vapor transport and condensation method [28]. In spite of the accomplishment of an awful lot of In$_2$O$_3$ nanostructures, the reports related to IndiumOxy-Nitride nanoparticles,

nanochains and even the unprecedented loquat-like nanostructures and their optical

properties of In_2O_3 are still limited and even unseen. Thus, my passion to delve into

the investigation is ignited from this point.

Chapter 2   Theoretical background and experiment apparatus

2-1 Growth mechanism of one-dimensional Indium Oxide

Among all vapor-based methods, the VLS process seems to be the most successful for generating 1D nanostructures with single-crystallinity and in relatively large quantities. This process was originally developed by Wanger and coworkers to produce micrometer-sized whiskers in 1960s [28], and recently reexamined by Lieber [29], Yang [30], and many other research groups to generate nanowires and nanorods from a enormous variety of compound semiconductors. A typical VLS process starts with the dissolution of gaseous reactants into nanosized liquid droplets of a catalyst metal, followed by nucleation and growth of single-crystalline rods and then wires. The 1D growth is mainly induced and dominated by the liquid droplets, the sizes of which remain essentially unchanged during the entire process of wire growth. In this sense, each liquid droplet serves as a soft template to strictly constrain the lateral growth of an individual wire. As a major requirement, there should exist a good solvent capable of forming liquid alloy with the target material, ideally they should be able to form eutectic compounds.

However, one of the challenges confronted with the VLS process is the selection of an appropriate catalyst working with the solid material to be processed into 1D nanostructures. Presently, this is done by analyzing the equilibrium phase diagrams. It

has also been shown the analysis of catalyst and growth conditions can be substantially simplified by considering the pseu-binary phase diagram between the metal catalyst and the solid material of interest.

The following is a vivid example presented by Yang *et al.* [30], and all major steps involved in a VLS process are schematically illustrated in the Figure 2-1-1A with the growth of Ge nanorods as an example. According to the Ge-Au binary phase diagram (Figure 2-1-1B), Ge and Au form liquid alloys while the temperature is raised above the eutectic point (361 ^{o}C). Once the liquid droplet is supersaturated with Ge, nanowires or nanorods growth will begin to occur at the solid-liquid interface, as shown in Figure 2-1-2. Vapor pressure of Ge in the system has to be kept fairly low that secondary nucleation events will be thoroughly suppressed. Both physical methods (laser ablation, thermal evaporation, and sputtering) and chemical methods (chemical vapor transport and deposition) have been employed to generate the vapor species required for the growth of nanowires or nanorods, and no salient difference was found in the quality of such nanostructures produced by these methods.
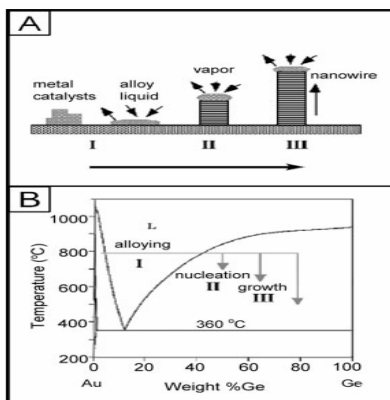
Fig. 2-1-1 (A) Schematic illustration showing the growth of a nanowire via the VLS mechanism. (B) The binary phase diagram between Au and Ge, with the indication of the compositional zones responsible for alloying, nucleation, and growth.
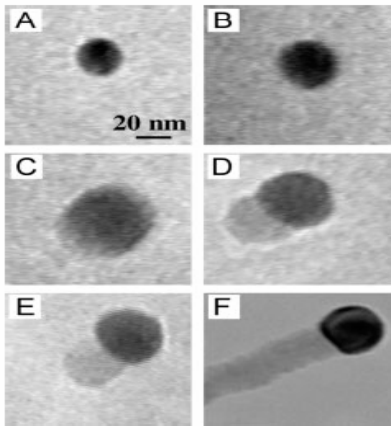
Figure 2-1-2 The birth of a Ge nanowire on a Au nanocluster, as observed using in-situ TEM. As following the increase in the liquid droplet (Ge-Au alloy) size during the Ge vapor condensation process, the droplet was supersaturated with Ge component. Simultaneously, a Ge nanowire grew out of this droplet and became longer as time elapsed.

2-2 Scanning Electron Microscope and Transmission Electron Microscope

Electron beam techniques are summarized in the Figure 2-2-1. Incident electrons are absorbed, emitted, reflected, or transmitted and can, in turn, cause light or X-ray emission. For our frequent investigation, the secondary electrons emitted from the specimen and the incident electrons transmitting the specimen are specially intriguing among those generated or inherent electrons. Incident electrons can be focused, deflected, and accelerated by appropriate potentials; they can be sufficiently detected and counted, their energy and angular distribution can be measured, and they do not contaminate the sample or the vacuum system. As the so-called nondestructive measurement, these electron beam measurements do good to morphology characterization. However, because they are charged, they can cause samples charging that may distort the measurement.
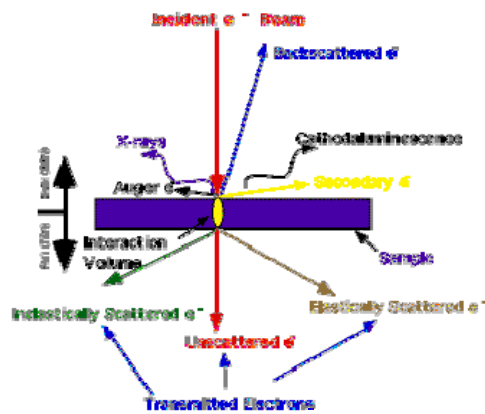
Fig. 2-2-1 Electron beam characterization techniques
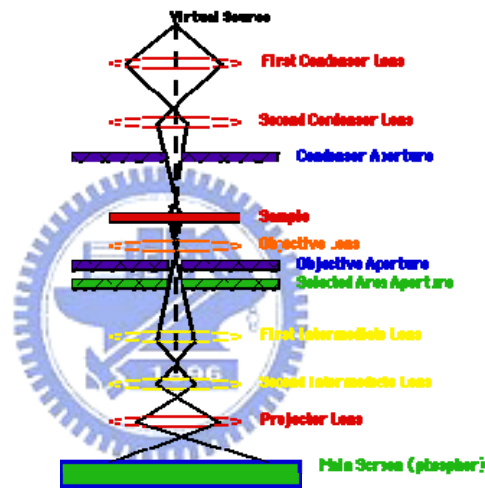
Fig. 2-2-2 Illustration of electron microscope system

The basic structure of both SEM and TEM is illustrated atop. The main spirit of the system is the electromagnetic optical system modulating the focus to form magnified image on the display.

A magnetic lens consists of a coil of copper wires inside the iron pole pieces. A current through the coils creates a magnetic field (symbolized by red lines) in the bore

of the pole pieces. The rotationally symmetric magnetic field is inhomogeneous in such a way that it is weak in the center of the gap and becomes stronger close to the bore. Electrons close to the center are less strongly deflected than those passing the lens far from the axis. The overall effect is that a beam of parallel electrons is focused into a spot (so-called cross-over).In a magnetic field, an electron experiences the Lorentz force F: The focusing effect of a magnetic lens therefore increases with the magnetic field B, which can be controlled via the current flowing through the coils. As it is described by the vector product, the resulting force **F** is perpendicular **v** and **B**. This leads to a helical trajectory of the electrons and to the magnetic rotation (image is rotated in respect of the object). Magnetic lenses influence electrons in a similar way as convex glass lenses do with light. Thus, very similar diagrams can be drawn to describe the respective ray paths. Consequently, the imaginary line through the centers of the lenses in an electron microscopes is called *optical axis* as well. Furthermore, the lens equation of light optics is also valid in electron optics, and the magnification of a lens is defined accordingly:

$1/u + 1/v = 1/f$ Magnification M $= v/u$

f: focal length; *u*: object distance; *v*: image distance

In electron microscopes, magnetic lenses perform two different tasks:
1. Beam formation (condenser lenses in TEM and SEM)
2. Image formation and magnification (objective, diffraction, intermediate, and projective lenses in TEM).

Right now, what I am going to discuss is the principle of useful electron beam characterization techniques used in my experiment:

1. Scanning Electron Microscopy:

An electron microscope utilizes an electron beam to produce a magnified image of the sample. There are three types of electron microscopes: scanning, transmission, and emission. In the scanning and transmission electron microscope, an electron beam incident on the sample produces an image while in the field-emission microscope the specimen itself is the source of electrons. SEM is similar to light microscopy with the exception that electrons are used instead of photons and the image is formed in the different manner. An SEM consists of an electron gun, a lens system, scanning coils, an electron collector, and a display (a CRT or an LCD), so does the TEM. The electron energy is typically 10-30 KeV for most samples, but for insulating samples the energy can be as low as several hundred eV. The use of electrons has two main advantages over optical microscopes: much larger magnifications are possible since electron wavelengths are much smaller than photon wavelengths and the depth of field is much larger. The image in an SEM is produced by scanning the sample with a focused electron beam and detecting the secondary or backscattering electrons. Electrons and photons are emitted at each beam location and subsequently detected. Secondary electrons form the conventional SEM image, backscattered electrons can

also form an image, X-rays are used to in the electron microprobe as to lead to the Energy Dispersive Spectroscopy, emitted light is known as cathodoluminescence, and absorbed electrons are measured as electron-beam induced current. All of these signals can be detected and amplified synchronously via the scanning coil and then forming magnified images on the display.

2. Transmission Electron Microscopy

With the similar structure and more powerful function compared with SEM, TEM offers the in-depth perspective of specimen characterizations. There are three primary imaging mode, listing as bright-field, dark-field, and high resolution microscopy. Image contrast does not depend very much on absorption, as it does in optical transmission microscopy, but rather on scattering and diffraction of electrons in the samples. Images formed using only the transmitted electrons are bright-field images and images formed using a specific diffracted are dark-field images. Few electrons are absorbed in the sample. Absorbed electrons lead sample to sample heating to change the sample during the measurement.

The objective lens forms a diffraction pattern in the back focal plane with electrons scattered by the sample and combines them to generate an image in the image plane (1. intermediate image). Thus, diffraction pattern and image are

simultaneously present in the TEM. It depends on the intermediate lens which of them

appears in the plane of the second intermediate image and magnified by the projective

lens on the viewing screen. Switching from real space (image) to reciprocal space

(diffraction pattern) is easily achieved by changing the strength of the intermediate

lens. In imaging mode, an objective aperture can be inserted in the back focal plane to

select one or more beams that contribute to the final image (BF, DF, HRTEM). In

selected area electron diffraction (SAED), an aperture in the plane of the first

intermediate image defines the region of which the diffraction is obtained. As shown
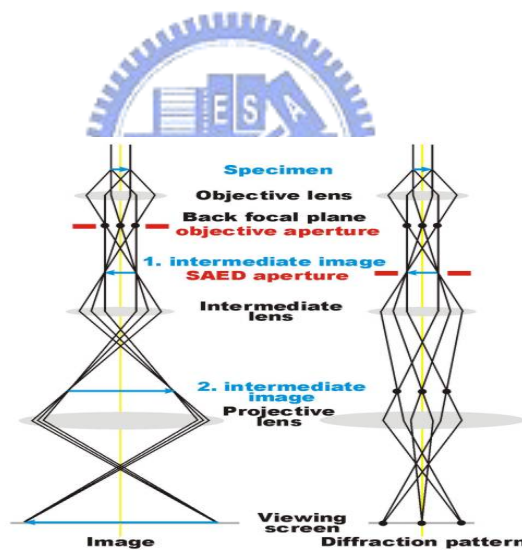
in below.

Fig. 2-2-3 Schematic of imaging of TEM

In the bright field (BF) mode of the TEM, an objective aperture is placed in the

back focal plane of the objective lens which allows only the direct beam to pass. In

this case, mass-thickness and diffraction contrast contribute to image formation: thick

areas, areas in which heavy atoms are enriched, and crystalline areas appear with dark

contrast. In spite of the useful information obtainable from BF images, it should be

mentioned that the interpretation of contrast is often impeded since these phenomena

occur simultaneously.

In dark field (DF) images, one or more diffracted beams are allowed to pass the

objective aperture. The direct beam is blocked by the aperture. In contrast to the direct

beam, the diffracted beam has interacted strongly with the specimen, and often very

useful information is present in DF images, e.g., about planar defects, stacking faults

or particle size.

To obtain lattice images, a larger objective aperture has to be selected that allows

many beams including the direct beam to pass. The image is formed by the

interference of the diffracted beams with the direct beam (phase contrast). If the point

resolution of the microscope is sufficiently high and a suitable sample oriented along

a zone axis, then high-resolution TEM (HRTEM) images are obtained. In many cases,

the atomic structure of the specimen can directly be investigated by HRTEM.

The incident parallel electron wave interacts elastically while passing through the

specimen, and the resulting modulations of its phase and amplitude are present in the

electron wave leaving the specimen. The wave here, the object exit wave o(r), thus

contains the information about the object structure. The objective lens performs

1. the Fourier transform (Fourier analysis) that creates the diffraction pattern of the object in the back focal plane and 2. the inverse Fourier transform (Fourier synthesis) that makes the interference of the diffracted beams back to a real space image in the image plane (lattice image).

2-3 Energy Dispersive X-ray Spectroscopy (EDS) and Selected Area Electron Diffraction (SAED)

EDS and SAED are two auxiliary function affiliated to SEM/TEM and TEM respectively. Both of them are used to characterize samples based on the constituents and structures. **Energy dispersive X-ray spectroscopy** (EDS or EDX) is an analytical tool predominantly used for chemical characterization. Being a type of spectroscopy, it relies on the investigation of a sample through interactions between light and matter, analyzing X-rays in its particular case. Its characterization capabilities are due in large part to the fundamental principle that each element of the periodic table has a unique electronic structure and, thus, a unique response to electromagnetic waves. The excess energy of the electron that migrates to an inner shell (in order to fill the newly-created hole) can do more than emit an X-ray. Often, instead of X-ray emission, the excess energy is transferred to a third electron from a

further outer shell, prompting its ejection. This ejected species is called an Auger electron, and the method for its analysis is known as Auger Electron Spectroscopy (AES). X-ray Photoelectron Spectroscopy (XPS) is another close relative of EDS, utilizing ejected electrons in a manner similar to that of AES. Information on the quantity and kinetic energy of ejected electrons is used to determine the binding energy of these now-liberated electrons, which is element-specific and hence allows chemical characterization of a sample. EDS is often contrasted with its microscale spectroscopic counterpart, WDS (Wavelength-Dispersive X-ray Spectroscopy). WDS differs from EDS in that it uses the diffraction patterns created by light-matter interaction as its raw data.

Selected area Electron diffraction, abbreviated as SAED, is a crystallographic experimental technique that can be performed inside a transmission electron microscope (**TEM**).

In a TEM, a thin crystalline specimen is subjected to a parallel beam of high-energy electrons. As TEM specimens are typically ~100nm thick, and the electrons typically have an energy of 100-400 kiloelectron volts, the electrons pass through the sample easily. In this case, electrons are treated as wave-like, rather than particle-like (see wave-particle duality). Because the wavelength of high-energy

electrons is a fraction of a nanometer, and the spacings between atoms in a solid is only slightly larger, the atoms act as a diffraction grating to the electrons, which are diffracted. That is, some fraction of them will be scattered to particular angles, determined by the crystal structure of the sample, while others continue to pass through the sample without deflection.

As a result, the image on the screen of the TEM will be a series of spots -- the **selected area diffraction pattern**, SADP, each spot corresponding to a satisfied diffraction condition of the sample's crystal structure. If the sample is moved under the beam, bringing different sections of it under illumination, the arrangement of the spots in the diffraction pattern will change. If the sample is tilted, the same crystal will stay under illumination, but different diffraction conditions will be activated, and different diffraction spots will appear or disappear.

SAD is referred to as "selected" because the user can easily choose which part of the specimen to obtain the diffraction pattern from. Located below the sample holder on the TEM column is a **selected area aperture**, which can be inserted into the beam path. This is a thin strip of metal that will block the beam. It contains several different sized holes, and can be moved by the user. The effect is to block all of the electron beam except for the small fraction passing through one of the holes; by moving the
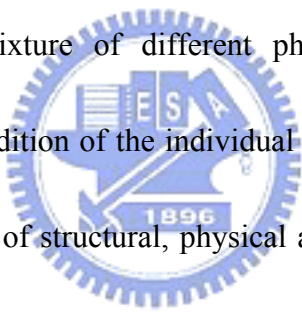
aperture hole to the section of the sample the user wishes to examine, this particular area is selected by the aperture, and only this section will contribute to the SADP on the screen. This is important, for example, in polycrystalline specimens. If more than one crystal contributes to the SADP, it can be difficult or impossible to analyze. As such, it is useful to select a single crystal for analysis at a time. It may also be useful to select two crystals at a time, in order to examine the crystallographic orientation between them.

As a diffraction technique, SAED can be used to identify crystal structures and examine crystal defects. It is similar to x-ray diffraction, but unique in that areas as small as several hundred nanometers in size can be examined, whereas x-ray diffraction typically samples areas several centimeters in size.

2-4 X-ray diffraction

X-ray diffraction (XRD) is a versatile, non-destructive technique that reveals detailed information about the chemical composition and crystallographic structure of natural and manufactured materials. A crystal lattice is a regular three-dimensional distribution (cubic, rhombic, etc.) of atoms in space. These are arranged so that they form a series of parallel planes separated from one another by a distance d, which

varies according to the nature of the material. For any crystal, planes exist in a number of different orientations --- each with its own specific *d*-spacing. When a monochromatic X-ray beam with wavelength *lambda* is projected onto a crystalline material at an angle *theta*, diffraction occurs only when the distance traveled by the rays reflected from successive planes differs by a complete number *n* of wavelengths. By varying the angle *theta*, the Bragg's Law conditions are satisfied by different *d*-spacings in polycrystalline materials. Plotting the angular positions and intensities of the resultant diffracted peaks of radiation produces a pattern, which is characteristic of the sample. Where a mixture of different phases is present, the resultant diffractogram is formed by addition of the individual patterns. Based on the principle of X-ray diffraction, a wealth of structural, physical and chemical information about the material investigated can be obtained. A host of application techniques for various material classes is available, each revealing its own specific details of the sample studied. Generally, XRD offers three types of scan: *theta/2theta*, rocking curve, reciprocal space mapping. The following is a basic XRD measurement setup derivation of Bragg's law and an example for Body-Centered Cubic (BCC) characterization (Indium Oxide belongs to BCC.).
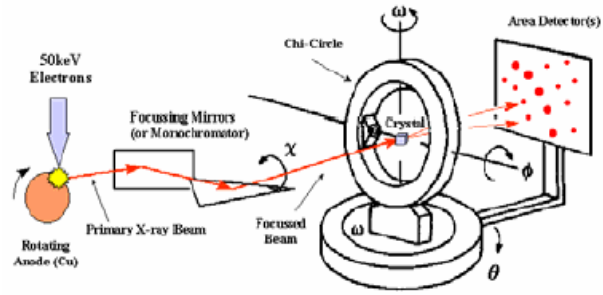
Fig. 2-4-1 Schematic of a basic X-ray diffractor setup.
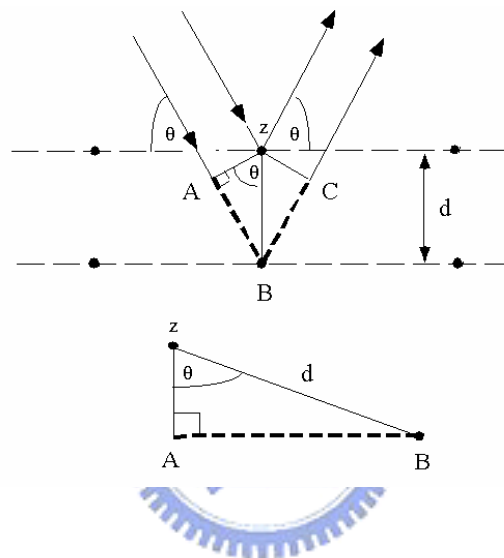
Fig. 2-4-2 Deriving Bragg's Law using the reflection geometry and applying trigonometry. The lower beam must travel the extra distance (AB + BC) to continue traveling parallel and adjacent to the top beam. (2dSin θ =n λ)
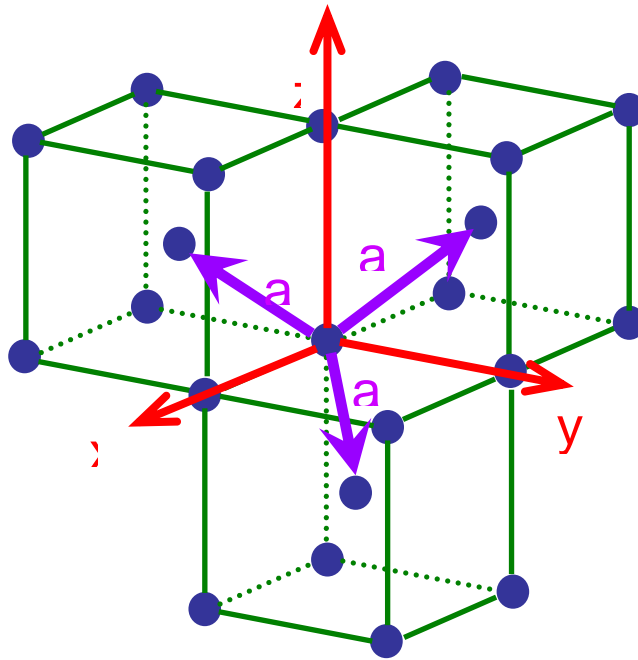
Fig. 2-4-3 The unit cell of Body-Centered Cubic.

The equation for the body-centered cubic structure is

$$\frac{1}{d^2} = \frac{(h^2 + k^2 + l^2)}{a^2} \qquad \text{(eq. 2-4-1)}$$

Combining with Bragg's law ($2d\mathrm{Sin}\,\theta = \lambda$) with eq. 2-4-1 yields

$$\frac{\mathrm{Sin}^2\theta}{(h^2 + k^2 + l^2)} = \frac{\lambda^2}{4a^2} \qquad \text{(eq. 2-4-2)}$$

Rearranging eq. 2-4-2 gives

$$\mathrm{Sin}^2\theta = \frac{\lambda^2}{4a^2}\,(h^2 + k^2 + l^2) \qquad \text{(eq. 2-4-3)}$$

Thus the lattice constants can be estimated from the above derivation.

2-5 Photoluminescence

Photoluminescence is a process in which a chemical compound absorbs photons (electromagnetic radiation), thus transitioning to a higher electronic energy state, and then radiates photons back out, returning to a lower energy state. Technically, it is "luminescence arising from photoexcitation". The period between absorption and emission is typically extremely short, on the order of 10 nanoseconds. Under special circumstances, however, this period can be extended into minutes or hours.

Photoluminescence spectroscopy is a contactless, nondestructive method of probing the electronic structure of materials. Light is directed onto a sample, where it is absorbed and imparts excess energy into the material in a process called photo-excitation. One way this excess energy can be dissipated by the sample is through the emission of light, or luminescence. In the case of photo-excitation, this luminescence is called photoluminescence. The intensity and spectral content of this photoluminescence is a direct measure of various important material properties.

Ultimately, available chemical energy states and allowed transitions between states (and therefore wavelengths of light preferentially absorbed and emitted) are determined by the rules of quantum mechanics. A basic understanding of the principles involved can be gained by studying the electron configurations and

molecular orbitals of simple atoms and molecules. More complicated molecules and advanced subtleties are treated in the field of computational chemistry.

The following (Figure 2-5-1) is the schematic setup for PL system with a He-Cd operating at 25mW at the line of 325 nm.
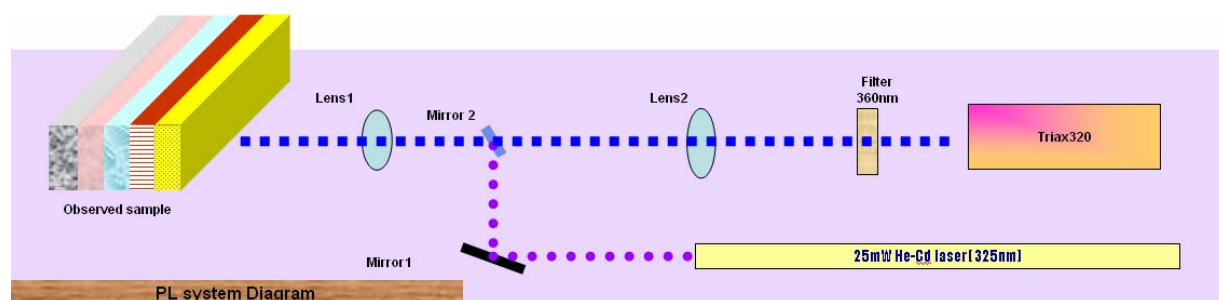
Fig. 2-5-1 Schematic setup for PL system.

Hereby, I am going to introduce some fundamental transitions usually occur in the compound semiconductors, especially oxide compounds.

Because samples is excited with an optical source, typically a laser enrggy $> E_g$ which generates electron-hole pairs (ehps), recombining by one of several mchanisms. Photons are emitted for radiative recombination. And photons are not emitted for nonradiative recombination in the bulk or at the surface. Some of the photons may be absorbed in the sample, provided the photons are directed to the back surface may be reflected and emitted. The photon energy is dependent on the recombination process, illustrated in the figure below (Fig. 2-5-2).
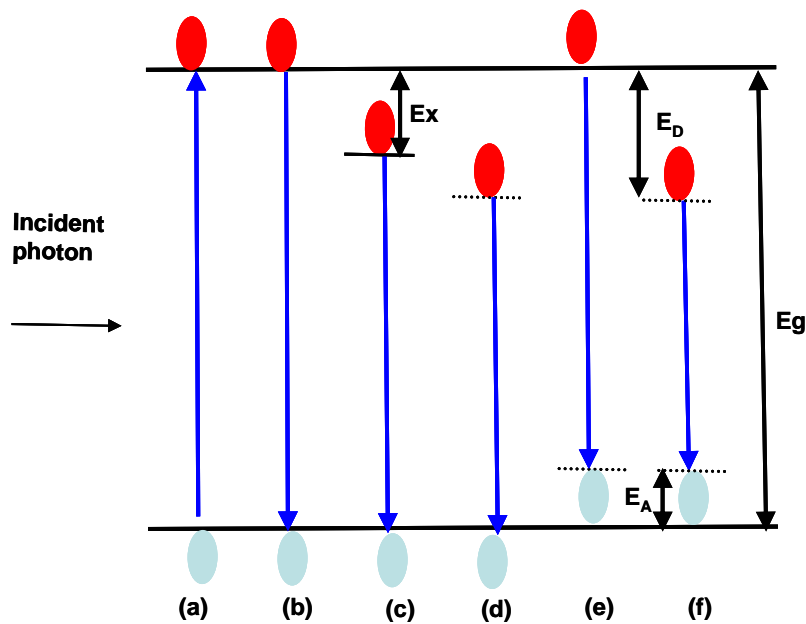
Fig. 2-5-2 The band diagram of possible routes to radiative recombination.

Band-to-band recombination (Fig. 2-5-2 (b)) dominates at room temperature but it is rarely observed at low temperatures in materials with small effectives according to the large electron orbital radii. Nevertheless, when a photon generates an ehp, Coulomb attraction can result in the formation of excitonic state (a kind of excited state beneath the conduction band in the midst of the forbidden gap)in which an electron and a hole remain bound to one another. This kind of two elementary particles interaction is referred to a free exciton. Simply put, the electron hole pair binding leads to an exciton as shown in (Fig. 2-5-2 (c)). Its energy is less than the bandgap energy by Ex (excitonic binding energy). An exciton can move freely through the crystal, but because it's a bound ehp, both electron and hole move simultaneously with each other and neither photoconductivity nor current takes place. However, a free hole can combine an electron on a neutral donor (Fig. 2-5-2 (d)) to

form a positively charged excitonic ion or the so-called donor bound exciton. The electron bound to the donor travels in a wide orbit about the donor. Likewise, electrons combining with a hole on neutral acceptors also form acceptor bound excitons, see Fig. 2-5-2 (e). Simply stated, as long as the semiconductor is less pure, the bound exciton recombination dominates over free exciton recombination. Let's consider some indirect bandgap materials, though they don't emit photons easily, once they emit the emissive energy must comply with the inclusion of phonon energy. That is, emissive energy = Eg-Ex-Ep, where Ep is the phonon energy. Ultimately, I have to combine all the conditions, i.e. the semiconductor is filled with impurity states. In order to give the simple case, I take only one donor and one acceptor into account (fig. 2-5-2 (f)). In this case, an electron on a neutral donor can recombine with a hole on a neutral acceptor, and this is the well known donor-acceptor (D-A) recombination. The emissive energy should be modified by the Coulomb attraction between donors and acceptors. Hence, the emissive energy becomes:

$$Eg-(E_A+E_D)+q^2/4\Pi \varepsilon r$$

where r is the distance between a donor and an acceptor. To be noted, the emissive photon energy can be higher than the bandgap in the heavily doping condition.

2-6 Furnace

This is a furnace with two-zone temperature controllers. And there are two kinds of gases provision. One is Nitrogen and the other is Oxygen. Attached to the end of the tube is a mechanical pump, which can exert itself to exhaust the air inside the quartz tube to the extent of 0.01 Torr. In my experiments, my samples were grown via the VLS and VS mechanism.Thus, preparing substrates with gold nanoparticles as catalysts was the first step. The research is in the scope of semiconductor nanostructure characterization and optical characteristics analyses. Looking forward to form oxide compound semiconductor nanostructures is substantially achieved. The following chapter will discuss profoundly about the product of my furnace and the characterization results. Below the passage is the schematic figure of the furnace.
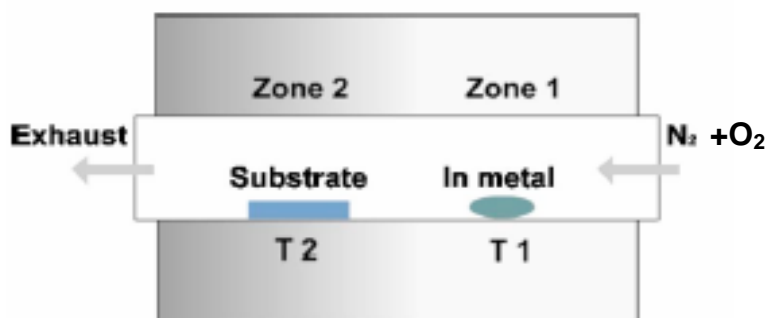

Fig. 2-6-1 Schematic of the furnace setup.

Chapter 3　　　Experimental Process, Results and Discussion

Because my research is based on structural and optical characteristics of the compound semiconductor of Indium Oxide nanostructures, the following three main studies will be discussed hereafter. Since I want to form nanowire like structure, I start with Vapor-Solid technique to Vapor-Liquid-Solid technique in order to accomplish the goal and analyze the relevance. In addition, I place each of them in the section of 3-1, 3-2 and 3-3 individually. And the titles of these three sections are named after the distinct morphologies and optical emissive properties. We could see as follows,

3-1 Observation of strong red photoluminescence with broadband in indium oxynitride nanoparticles

3-2 Synthesis of In2O3 nanocrystal chains and annealing effect on their optical properties

3-3 Thermally evaporated In_2O_3 nanoloquats with tunable broad band emissions

In each section, the content will begin with the samples preparation, results of all the characterizations and wind up with the discussion and conclusion of the phenomena of these nanostructures exhibit structurally and optically.

3-1 Observation of strong red photoluminescence with broadband in indium oxynitride nanoparticles

Indium oxy-nitride nanoparticles were synthesized on silicon substrate in

nitrogen atmosphere using a method involving a thermal evaporation of pure indium in a two-zone reactor. Nanoscale compositional analysis by energy dispersion spectrum shows the existence of indium oxy-nitride compound. X-ray diffraction analysis further confirms high crystallization and nitrogen atoms existence within the nanoparticles. Scanning electron microscopy investigations shows shape transformation from amorphous sphere to well-shaped octahedron with an average nanoparticle size from 50 nm to 1 μm when growth temperature of substrate increased from 600 to 900 °C. Photoluminescence study was performed on indium oxy-nitride nanoparticle samples grown at different temperatures. The emission intensity increases with growth temperature suggesting the formation of high quality indium oxy-nitride nanoparticles with increasing temperature. It was observed that these nanoparticles grown at 900 ℃ could emit a strong photoluminescence spectrum centered around 700 nm with a board full width at half maximum of about 250 nm, spanning the whole red band.
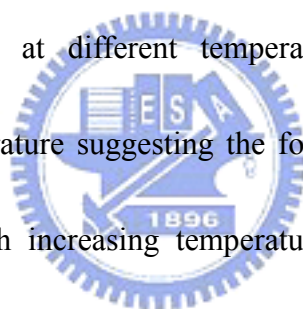
3-1-1 Samples preparation and growth

The experimental setup for synthesis of indium oxynitride nanoparticles is depicted schematically in the experimental apparatus section. The starting material, 3 g indium metal, was placed in a quartz boat located inside an 8 cm diameter quartz tube reactor,

referred to as zone 1 with the temperature setting as $T1$. p-type silicon (100) substrates

were placed at the downstream of the tube reactor separated from the starting material

by 20 cm, which was referred to as zone 2 with the temperature setting as $T2$. The

quartz tube was degassed by a mechanical pump down to 10^{-2} torr and then purged

with the nitrogen flow of 150 sccm (cubic centimeter per minute at STP) as the source

of nitrogen atoms. During the growth process, we fixed $T1$ to be 900 °C to promote

pyrolysis of nitrogen molecules and the indium metal. $T2$ in zone 2 was adjusted from

600 to 900 °C. The typical reaction time was about 30 min. The dependence of the

reaction time has also been examined and adjusted to 150 min for $T2$=900 °C. The

synthesized nanoparticles on Si substrates were unloaded after the reactor was cooled

down.
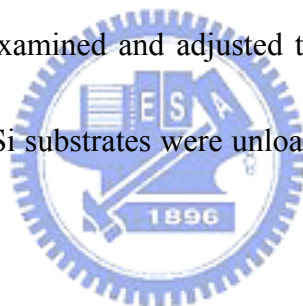
3-1-2 Structural and optical charaterizations

The morphologies and composition of the as-grown samples were characterized

by field emission scanning electron microscopy (SEM, JEOL 6500F) and energy

dispersive x-ray spectrometry (EDS). The structure analysis was also performed by

the x-ray diffraction (XRD) measurement with Cu Kα radiation. Photoluminescence

(PL) spectra were measured at room temperature by means of TRIAX-320

spectrometer using a 25 mW He-Cd laser with the emission wavelength of 325nm as

the excitation source.

A typical SEM image of indium oxy-nitride nanoparticles with well-shape octahedron grown on a Si substrate is shown as Fig. 3-1-1(a). This image shows that the dimensions of these nanoparticles with well-shaped octahedron range from 50 to 1000 nm, which could relate to the unstable atmosphere and temperature distribution in the reactor. The morphology of nanoparticles is similar to the indium oxide nanoparticles reported by Y. Zhang *et al.* [31]. EDS measurements performed on the nanoparticles indicate that the main composition of these nanoparticles is indium, with few oxygen and nitrogen existing as shown in Fig. 3-1-1(b). EDS didn't detect nitrogen from the sample grown without placing starting material indium, which indicates nitrogen atom has not reacted with Si substrate. Therefore, the formation of indium oxy-nitride nanoparticles was confirmed in terms of the EDS result.

The typical XRD pattern of indium oxy-nitride nanoparticles was shown in Fig. 3-1-2. The sharp and symmetric peak at (222) plan implies the crystallization in indium oxy-nitride is superior and rather than the polycrystalline. All the diffraction peaks can be indexed to a pure cubic phase structure with lattice constant of a = 0.995 nm in spite of a little nitrogen incorporation, which is slightly different from the literature value of indium oxide with lattice constant a = 1.011 nm (JCPDS 71-2195). The peaks of the (222), (400) and (411) for the indium oxide from the standard value

(JCPDS 71-2195) are 30.585°, 35.462° and 37.692°, relatively. Our XRD result shows

the peaks of the (222), (400) and (411) shifted to 31.121°, 35.465° and 38.195°, which

is reasonable when the smaller nitrogen atoms replaced the oxygen atom. Therefore,

the lattice constant of indium oxy-nitride is smaller than the standard value of indium

oxide. The XRD results indicate the incorporation of nitrogen is consistent with EDS

analysis. The relatively strong (222) diffraction suggested that the crystal might be

truncated by {111} crystal face.

In our growth condition, there are a great deal of indium oxy-nitride octahedral

nanoparticles found in the down stream when In chunks were heated at 900 ℃. The

low evaporation pressure of indium even at the high temperature has the advantages

of one–dimensional nanomaterial growth as reported by Zhang *et al.* [32]. Since no

catalyst on Si substrates was used, we suggest the growth of indium oxy-nitride

octahedrons may be due to the vapor-solid (VS) mechanism. Indium vapor generated

at high temperature and combined with oxygen and nitrogen atoms to form special

shaped indium oxy-nitride and then deposited on the Si substrates at Zone 2.

Fig. 3-1-3 (a)~(d) shows the indium oxy-nitride nanoparticles grown at different

temperature of Zone 2 from 600 to 900 ℃, respectively. The average size of

nanoparticles gradually increased from 50 nm to 1 μm. The transformation from

amorphous to well-shape octahedron with increasing growth temperature can be

observed clearly. In addition, the amount of nanoparticles increased and aggregated closer and closer. There are two aspects could be considered. First, the indium vapor from Zone 1 could gain high thermal energy at 900 ℃ to bind with oxygen and nitrogen. Then, the formed indium oxy-nitride deposited on the Si substrates in Zone 2. Second, the shape transformation implies effect of annealing is notable at the higher growth temperature. In general, crystal structure repair and ion activation often take place during the annealing process. In other words, most defects will be pruned and the quality will be improved after annealing. Therefore, we suggest that the crystal growth and repair were occurred at the same time. The photoluminescence spectrum of the indium oxy-nitride nanoparticles with different growth temperature was measured at room temperature. Fig. 3-1-4 shows the strong and broad PL emission spectrum recorded from the indium oxy-nitride nanoparticles with different growth temperature, which is mainly located in the orange color band with the peak wavelength centered around 610 nm. The emission intensity increases when the samples were grown with increasing temperature, which also suggests the higher quality indium oxy-nitride nanoparticles formed at higher temperature.

Moreover, the influence of growth time extending from 30 to 150 min was investigated when T1 and T2 were both 900 ℃. Fig. 3-1-5 shows the PL spectrum from the indium oxy-nitride nanoparticles when the growth time was extending to 150

min. A broad PL emission band centered around 700 nm was found with a full width

at half maximum (FWHM) of about 250 nm, spanning the whole red region. The

broad FWHM of the PL spectrum could be due to the thermal excitations and the

broad size distribution of the nanoparticles. Nitrogen flow is found to be very

important to grow nanomaterials in this CVD system. Carrier gas frequently affects

the morphology and quality of products in similar experiments. However, how the

flow affects the morphology in the present work needs further study. In the previous

investigations, Zhou *et al.* had reported PL peaks at 480 and 520 nm observed from

indium oxide nanoparticles [33], and Lee *et al.* had reported PL peak at 637 nm

observed from indium oxide film [34]. According to these reports, the emission

mechanism was mainly attributed to the effect of the oxygen deficiencies. As a result,

gradually increasing temperature could make the oxygen deficiencies decrease, and

decrease the intensity of PL emission. However, the intensity of the PL emission in

these indium oxy-nitride nanoparticles was increased as the growth temperature was

increased. Therefore, the emission couldn't results from the radioactive recombination

of a photo-excited hole with an electron occupying the oxygen vacancies. The

possibility of the observed PL arising from a quantum confinement effect could be

also excluded because the exciton Bohr radius for the indium oxide is estimated to be

in the range between 2.6 and 5 nm [33], which is far smaller than the dimension of
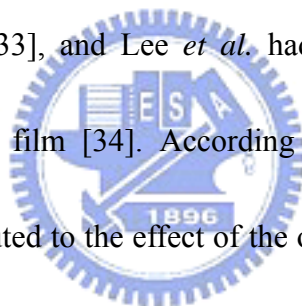
these indium oxy-nitride nanoparticles. To conclude above assertations, the photon could be emitted by the transition of an excited carrier from the conduction band to the valence band of indium oxy-nitride nanoparticles along a radiative recombination path. Contrary to the result in Fig. 3-1-4, not only the FWHM increases but also the central peak red-shifts about 100 nm. The inset figure reveals the SEM image of nanoparticles grown for 150 min. The well-shape octahedron still be hold but the reduced size of nanoparticles of about to 300~500 nm could be due to the partly dissociation of indium oxy-nitride causing the slight increase of the N/O ratio of these indium oxy-nitride nanoparticles as extending the growth time.
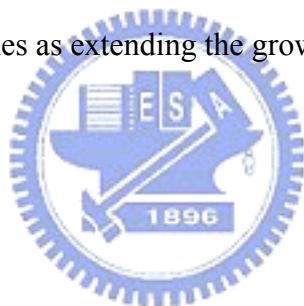
3-1-3 Summary

We have synthesized indium oxy-nitride nanoparticles by using a thermal evaporation method in a two-zone reactor. EDS and XRD analysis results confirm the composition and the crystal form of the indium oxy-nitride compound. SEM investigations show shape transformation from amorphous sphere to well-shaped octahedron with an average nanoparticle size from 50 nm to 1 μm when the growth temperature increased from 600 to 900 °C. The room temperature PL spectra of the nanoparticles with different growth temperatures showed light emission in the orange band, which may be related to the band-to-band transition. The PL spectrum could be

further extended to 700 nm with a broad FWHM of about 250 nm, spanning the whole

red region when the indium oxy-nitride was grown with the extension of the growth

time. The PL results indicate the indium oxy-nitride nanoparticles have potentials in

developing the red phosphor system for lamp applications.

3-2 Synthesis of In2O3 nanocrystal chains and annealing effect on their optical

properties

The synthesis of indium oxide nanocrystal chains on silicon substrates used gold

nanoparticles as catalyst on native silicon dioxide. Scanning electron microscopy

investigations showed In_2O_3 nanocrystal chains were formed. The nanocrystal chains

consisted of many well-shape octahedron nanoparticles with their size ranging from

20 nm to 100 nm connected with each other to form a network. Both high resolution

transmission electron microscopy and diffraction pattern revealed that the In_2O_3

nanocrystal chains were single crystalline grown along [111] direction.

Photoluminescence study of In_2O_3 nanocrystal chains exhibited main photoemission

at 544 nm due to the recombination between electrons in localized state induced by

oxygen vacancies and photogenerated holes in the valence band. After the annealing

treatment, the main photoluminescence peak not only slightly red shifted to 558 nm

but also became narrower, which was ascribed to the total localized states away from

the conduction band due to defect reduction and crystal repairing.

3-2-1 Samples preparation and growth

Single crystal (001) oriented silicon wafers were used as substrates. Gold nanoparticles having diameters of ca. 20 nm were used as catalysts; they were produced by the chemical reduction of gold chloride tetrahydrate ($HAuCl_4$) with sodium citrate, and then spread onto a silicon wafer coated with a native oxide layer using a self-assembled monolayer of 3-aminopropyltrimethoxysilane (APTMS) as an adhesion agent. Observed from the SEM images, the Au nanoparticles are 10~20 nm in width and the density is around 6×10^8 cm^{-2}. A two-zone vacuum furnace was used to grow the nanochains. Nitrogen was the carry gas and flowed through the system at rate of 30 sccm. During the growth process, 2 g indium powders were positioned upstream with the samples placed downstream. The source vapor was transported by the carrier gas and condensed on the substrates. The temperatures were heated to 900 ℃ for sources and 700 ℃ for samples. The typical reaction time was 6 hours and the growth pressure was around 0.1 torr.

3-2-2 Structural and optical charaterizations

The morphology and microstructure of the samples were investigated by scanning electron microscopy (JEOL, JSM 6500F) and high resolution transmission

electron microscopy (HRTEM, JEOL, JEM 2010F, operating at 200 kV). The compositions were analyzed using energy dispersive spectrometry (EDS) affiliated to the SEM. The selected area electronic diffraction pattern confirmed crystal orientation of In_2O_3 nanochains. Afterwards, the samples were furnace-annealed in the temperature of 700 °C for 2 hours in the oxygen ambience. The crystal structure analysis was performed by the XRD measurement with Cu Kα as radiation source. Photoluminescence (PL) spectra were measured at room temperature by means of TRIAX-320 spectrometer using a 25 mW He-Cd laser with the linewidth of 325 nm as the excitation source.
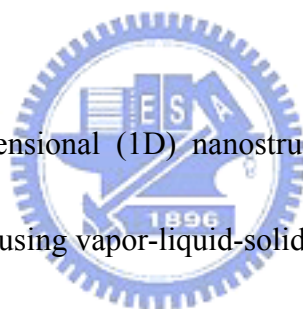
In general, for one-dimensional (1D) nanostructure growth, many researches have shown that the synthesis using vapor-liquid-solid (VLS) mechanism could obtain a constant diameter or periodically changing diameter along the growth direction without presence of many nanocrystals with different sizes [34~36]. In contrast, we obtained sensationally self-assembled In_2O_3 nanocrystal chains with many nanoparticles of different sizes when the growth pressure was 0.1 torr and the temperature was 700℃. Fig. 3-2-1(a) and (b) show these self-assemble In_2O_3 nanochains and net works. The nanochains have diameters of between 20 and 100 nm and length of around a few micrometers. They were connected with each other to form a complicated nano networks. A large number of the nanoparticles of the chains

would aggregate near the network junctions. P. Yang *ea al.* grew MgO nanochains and suggested that such morphology of nanochains were grown by a vapor-solid (VS) mechanism [37]. Based on our experiment results, we found the gold catalyst is necessary for the synthesis of the networks. However, we also observed many gold nanoparticles distributed on the substrate surface, which means the indium vapor from the upstream formed alloy with several gold nanoparticles, meanwhile, there were also many clustered octahedral In_2O_3 nanoparticles randomly dispersed on the substrate surface. In our growth process, therefore, the VS mechanism and gold catalyst played very important roles. We suggested it was likely that small octahedral In_2O_3 nanoparticles were formed in the air and fell on the substrate in the first place. Consequently, the gold catalysts nucleated with the adjacent In_2O_3 nanoparticles to start nanochains growth. Once the latter indium vapor reacted with the remaining oxygen molecules near the original In_2O_3 nanoparticles/nanochains, there was high likelihood to form the string of In_2O_3 nanoparticles as long chains. We focused on different position of In_2O_3 nanochains to proceed EDS measurement. The EDS spectrum shown in the fig. 3-2-1(c), indicates that the nanochains were essentially composed of indium and oxygen. The silicon peak originates from the silicon substrate and no gold was detected, in this way, we speculated the gold may remain on the substrate. Lao *et al.* has grown In_2O_3 nanocrystal chains in similar shapes as
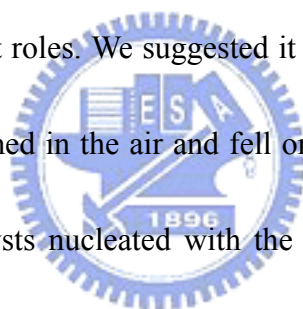
ours by using gold catalyst, meanwhile, they also found that there was no gold within

their nanochains structure [27].

Fig. 3-2-2(a) shows the selected TEM bright-field image of In_2O_3 nanochains.

The sizes of every particle in chains were different but the shapes were uniquely

octahedral. The junction boundary can be clear seen between the two nanoparticles.

Fig. 3-2-2(b) shows the high resolution TEM (HRTEM) image of one nanoparticle.

The corresponding selected area electron diffraction (SAED) is shown in fig. 3-2-2(c),

which proved our In_2O_3 nanochains were high-quality single crystals. Analyses of

both TEM images and SAED patterns revealed that the In_2O_3 nanochains are single

crystalline and grow along [111] direction.

We would further study the effect of thermal annealing with oxygen at 700 ℃

on the structure and optical characteristics of the In_2O_3 nanochains. The XRD patterns

of the In_2O_3 nanochains treated with and without thermal annealing are shown in fig.

3-2-3. The patterns correspond to In_2O_3 with the cubic structure with lattice constant

of a = 1.011 nm (JCPDS 44-1087). Both the XRD results revealed no additional peaks

corresponding to metallic indium or gold since no indium precipitated and it's

insensitive to detect the gold monolayer. We could see the same peaks occur in both

samples, which indicated the thermal annealing for the crystal orientation of the

sample could not cause obvious change. The high intensities with sharp contrast to the

background signal also indicated high crystallization quality of the In_2O_3 nanochains.

We measured the XRD (111) rocking curves in order to compare the quality between

both samples. The comparison is shown in fig. 3-2-4. The XRD line becomes stronger

and narrower as the samples treated with thermal annealing. However, there was no

clear difference in morphologies of both samples. The annealing effect could

generally facilitate ion activation and repair defects. In other works, most defects will

be pruned and the quality will be improved after annealing. Most of oxide

semiconductors are native n-type material since oxide vacancies [38]. Therefore, we

suggested that more oxygen atoms were filled into positions of vacancies when using

oxygen as carrier gas during annealing.
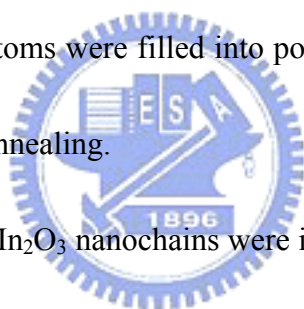
The optical properties of In_2O_3 nanochains were investigated by PL measurement.

The influence of thermal annealing on optical characteristics of In_2O_3 nanochains is

shown in fig. 3-2-5. Both PL intensity curves were normalized. After thermal

annealing treatment, not only the PL peaks of In_2O_3 nanochains red shifted from 544

to 558 nm but the full width of half maximal (FWHM) of PL spectrum also became

narrower. In additional, the integrated intensity of PL emission decreased abruptly

after annealing. Moreover, there was another peak occurred at 357 nm after annealing.

Since In_2O_3 is a semiconductor with a band gap of around 3.6 eV (344 nm), our 544

and 558 nm PL emission would not arise from the transition of excitons from the

conduction band to the valence band of In_2O_3 nanochains. On the other hand, the PL

peak of 357 nm might originate from the radiative recombination of an exited carrier

from the exciton state to the valence state. Many groups have studied on the optical

properties of In_2O_3 compound and they have obtained different results. Liang *et al.*

observed PL peaks at 470 nm from In_2O_3 nanofibers [39]. Li *et al.* measured PL of the

In_2O_3 nanotubes that exhibited emission of 593 nm [40]. Lee *et al.* observed PL peak

at 637 nm from In_2O_3 films [34]. The above PL mechanism was mainly attributed to

the effect of the oxygen deficiencies. The reason to the electronic n-type property of

In_2O_3 is that no enough oxygen atoms to catch electrons released from indium atoms.

Then that makes the donor level. The more free electrons exist in crystal, the smaller

transition path will be formed between the conduction band edge and the donor level

[41]. Hence both the PL peaks of 544 and 558 nm in our results demonstrated not only

deep-level emission ascribed to be defect-state-induced emission in In_2O_3 crystals, but

also redshift caused by lower defect and electron density after thermal annealing. That

fulfilled the consistency with the results of XRD.

A schematic diagram of relative states is shown in fig. 3-2-6. The E_L stands for

main localized state. The oxygen vacancies caused many localized states between the

conduction and valence band. The residual electrons in localized states would

decrease after thermal annealing and exhibit a narrower linewidth in the PL spectrum.

In the meantime, the decreased number of electrons in the localized state resulted in redshift of PL peak. An electron could be excited to the energy level higher than main localized states by a pumping source and further to form an exciton. Nevertheless, for oxide compound semiconductor, most native electrons attributed to oxide deficiencies would recombine with holes in the valence band swiftly, making the exciton emission less remarkable. Therefore, once fewer electrons were in localized states after thermal annealing in our case, there could be a higher opportunity of recombination between the electrons upper level and holes in the valence band for the emission peak of 357 nm. As for either this energy level is an exciton state or a general defect level state, further investigations remains to be conducted.

3-2-3 Summary

The nanocrystal chains comprised many well-shape octahedron nanoparticles with their size ranging from 20 nm to 100 nm connected to each other to form a network. We have discussed the growth mechanism and found crystalline grown along [111] direction by the analysis of TEM. PL study pointed out main photoemission at 544 nm due to the recombination between electrons in the localized state induced by oxygen vacancies and photogenerated holes in the valence band. After annealing treatment, the reduction of oxygen vacancies pushing the donor level

away from the conduction band could make the main emission peak not only red-shift to 558 nm but also show a narrower linewidth. Such self-assembled nanocrystal chains should have great potential for applications of novel optoelectronic devices and nano-photonics owing to their easy fabrication process and sensational high quality crystallinity.

3-3 Thermally evaporated In$_2$O$_3$ nanoloquats with tunable broad band emissions

The synthesis of the In$_2$O$_3$ nanoloquat grown under different oxygen flow rates and temperatures used the thermal evaporation method. The gold nanoparticles were used as the catalyst and were dispersed on the silicon wafer to assist the growth of In$_2$O$_3$ nanoloquats. The nanostructures of the In$_2$O$_3$ nanoloquats were characterized by scanning electron microscopy, transmission electron microscopy and x-ray diffraction. The photoluminescence (PL) study reveals that In$_2$O$_3$ nanoloquats could emit different luminescence peaks in the range 410~620 nm with broad band by tuning different oxygen flow rates and temperatures. The broad tuning range in the emission peaks of the In$_2$O$_3$ nanoloquats can be beneficial for possible applications in white light illumination.

3-3-1 Samples preparation and growth

The synthesis procedures of In_2O_3 nanoloquats started with gold nanoparticles produced by the chemical reduction of gold chloride tetrahydrate (HAuCl$_4$) with sodium citrate spread onto the Si substrates cleaned by the 3-Aminopropyl-trimethoxysilan (APTMS) ethanol solution and water. Observed from the SEM images, the Au nanoparticles are 10~20 nm in width and the density is around 6 X 10^8 cm^{-2}. Then, the gold nanoparticles on Si substrates were then sent to a two-zone vacuum furnace to grow the In_2O_3. In the two-zone vacuum furnace heated with two different temperatures, the 5 g indium powders were placed at the upstream source zone while the Si substrate was placed at the downstream reaction zone. The oxygen was used as the carrier gas. The source vapor was transported from the source zone by the carrier gas and condensed on the substrates in the reaction zone. We first adjusted oxygen flow rate from 50~200 sccm. The temperatures were set 900 ^{0}C for the source zone and 700 ^{0}C for the reaction zone. Then, we fixed the oxygen flow rate at 150 sccm and adjusted growth temperature from 500 to 900 ^{0}C in the reaction zone. The typical reaction time was 8 hours and the growth pressure was around 0.1 torr.

### 3-3-2 Structural and optical charaterizations

Scanning electron microscopy (SEM, by JEOL, JSM 6500F) and high-resolution transmission electron microscopy (HRTEM, by JEOL, JEM 2010F, operating at 200

kV) were used for investigation of the morphology and microstructure of the as-grown samples. The compositions were analyzed using energy dispersive spectrometry (EDS) attached to the SEM. Selected area electronic diffraction (SAED) confirmed the crystal orientation of In_2O_3 nanocrystals. The crystal structure analysis was performed by the XRD measurement with Cu Kα radiation. PL spectra were measured at room temperature with a spectrometer (TRIAX-320) excited by a 25-mW He-Cd laser with the emission wavelength of 325 nm.

Figure 3-3-1(c)~(f) show SEM images of the In_2O_3 nanocrystals grown at different oxygen flow rates in the range 50, 100, 150 and 200 sccm, respectively, by using the thermal oxidation method with the growth temperature of 700 ^{0}C. The name of In_2O_3 nanoloquat derives from special shapes of these nanocrystals similar to the real loquat fruits as shown in Fig. 3-3-1(a) and (b) [42]. The amount of nanoloquat was found to be dependent on the oxygen flow rate. As a result, Fig. 3-3-1(c) shows fewer nanoloquats existed and many In_2O_3 tips are beginning to sprout when the oxygen flow rate was 50 sccm. As the oxygen flow rate was increased to 200 sccm, most of In_2O_3 nanocrystals show well loquat shapes as indicated in Fig. 3-3-1(f).

The SEM images of the In_2O_3 nanoloquats grown at different temperatures ranged from 500 to 900 ^{0}C were shown in Figure 3-3-2 (a)~(c), respectively. It can be seen that the growth temperature has different impact on the morphology of the In_2O_3

nanoloquats. When the growth temperature was 500 ^{0}C, the evaporated nanocrystal

has a grain structure consisting of the granular and belted crystallites sized in about

100 nm. On the other hand, when the growth temperature was raised from 700 to 900

^{0}C, the loquat shape of In_2O_3 transformed into a pyramidal shape with clear crystal

faces. The bending or the curvature of the apexes of pyramids may arise from defects,

such as stacking faults and low-angle grain boundaries in the wall of the nanoloquats,

which may induce a different orientation growth [43]. Obviously, the growth

temperature in our experiment could affect the morphology and shape of In_2O_3

nanoloquats.
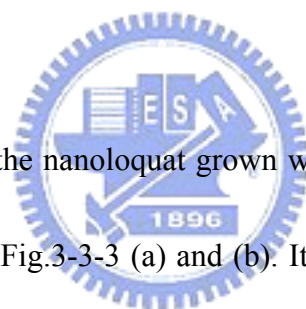
The HRTEM images of the nanoloquat grown with the oxygen flow rate of 150

sccm at 700 ^{0}C are shown in Fig.3-3-3 (a) and (b). It is clearly shown that the In_2O_3

nanoloquat was capped with a 20-nm gold nanoparticle. The presence of gold

nanoparticles at the top of the In_2O_3 nanoloquats provides strong evidence for a

vapor-liquid-solid (VLS) growth mechanism. However, VLS growth mechanism

generally leads to a well directional growth and further to form nanowire or nanorod

structures [44, 45], which is different from our results. We proposed that the short

In_2O_3 nanowires were nucleated at the gold nanoparticles by the VLS mechanism at

first. As the growth time passed by, the growth direction still favored to the top due to

the fast reaction provided by the catalyst. However, the over-supply of the indium

vapor interacting with oxygen atoms could further facilitate to enhance the lateral

growth rate, the lateral volume could increase and then turned into the loquat shape.

Figure 3-3-3(c), (d) shows HRTEM image of a partial In_2O_3 nanoloquat and the

corresponding SAED result, which proved our In_2O_3 nanoloquat was a single crystal

structure. The lattice plane of (422) with an interplanar spacing of 0.207 nm and (622)

with spacing of 0.153 nm can be obtained by the analysis of both TEM images and

SAED shown in Fig. 3-3-3 corresponding to the In_2O_3 crystal lattice planes

Typical XRD patterns of the In_2O_3 nanoloquats grown with different oxygen

flow rates and different growth temperatures are shown in Fig. 3-3-4 (a) and (b),

respectively. All the diffraction peaks could be indexed to a pure cubic phase structure

with a lattice constant of a = 1.011 Á(JCPDS 71-2195). Both measurement results

show that the stronger and sharper XRD phase peaks could be detected as the oxygen

flow rates and growth temperature were increased. As a result, the crystalline quality

of In_2O_3 nanoloquats could be improved by means of adjusting oxygen flows and

growth temperature, which were consistent with the SEM observations.

The normalized PL measurement results of the In_2O_3 nanoloquats prepared by

different growth conditions reveal the quality dependent characteristics as shown in

Fig. 3-3-5(a) and (b). Since the bandgap energy of In_2O_3 is around 3.6 eV, we could

boldly obviate the origin of the photoluminescence as shown in Fig. 3-3-5 from the

band-to- band transition. Namely, the transition could substantially be ascribed to the carrier recombination between the valence band and the oxygen vacancies induced donor levels formed in the midst of the In_2O_3 bandgap[47]. However, the different crystallization quality of the In_2O_3 nanoloquats could result in different transition path of carriers due to the different amounts of oxygen vacancies and defects generated during the growth [26]. Therefore, in our case, the worse quality would lead to a shorter wavelength emission due to more oxygen vacancies formed either the nanoloquats were grown in conditions of different oxygen flows or those of different growth temperatures. By adjusting these growth conditions, we could synthesize the In_2O_3 nanoloquats emitting different wavelength emission to span the whole visible light region. It is worth noting that the growth temperature influenced more prominently on the emission peak position than the oxygen flow. We could attribute the phenomenon to the significant role which growth temperature plays on the crystal atomic arrangement, demanding the energy supply from the growth temperature. In this way, the growth temperature has great impacts on the crystal quality and properties accompanying profoundly. which was also shown by Sundaram *et al.* that the concentration of oxygen vacancies dramatically depends on the heat treatment temperatures [46].

3-3-3 Summary

We have grown the In_2O_3 nanoloquat under different oxygen flow rates and temperatures using the thermal evaporation method. The VLS process mechanism was dominant in the growth of the In_2O_3 nanoloquats confirmed by the TEM images. The single crystal structures of the In_2O_3 nanoloquats were also characterized by the SEM, TEM and x-ray diffraction. The PL measurement results showed that In_2O_3 nanoloquats could emit different broadband luminescence peaks in the range of 410~620 nm by tuning oxygen flow rates and growth temperatures. Due to the different amount of oxygen vacancies prepared by different growth conditions, the optical transition energy of the In_2O_3 nanoloquats could become tunable, which could be beneficial for possible applications in white light illumination.
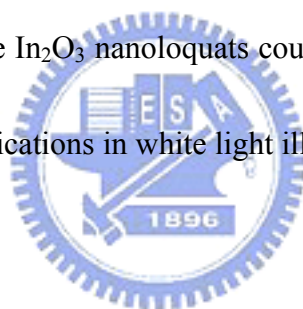
Chapter 4   **Conclusion**

I have successfully synthesized indium oxy-nitride nanoparticles, Indium Oxide nanochains, Indium Oxide nanoloquats by using a thermal vapor deposition method in a two-zone reactor. Apparently, the formation of these three nanostructures has paved the route toward the formation of Indium Oxide nanorods or nanochains. In addition, these three nanostructures are analyzed structurally and optically. Multitudes of analyses were carried out by XRD, EDS, SEM, TEM, and PL.

In the first part, the 50 nm to 1 um octahedral Indium Oxy-Nitride nanoparticles formed by Vapor-Solid mechanism exhibited great single crystallinity and the PL spectrum could be further extended to 700 nm with a broad FWHM of about 250 nm, spanning the whole red region as the Indium Oxy-Nitride was grown with the extension of the growth time. Simply put, these nanoparticles could be beneficial to red phosphor system for lamp applications.

In the second part, the well-shape octahedron Indium Oxide nanoparticles with their size ranging from 20 nm to 100 nm connected to one other forming a chain-like nanostructure. The complicated growth mechanism and the crystallinity were discussed in the preceding section. Furthermore, the annealing effect was investigated to explain the wavelength shift due to oxygen vacancies diminishing. Such self-assembled nanocrystal chains should have great potential for applications of

novel optoelectronic devices and nano-photonics owing to their easy fabrication process, sensational high quality crystallinity and wavelength modulation.

In the last part, it's the almost success toward forming Indium Oxide nanorods via the Vapor-Liquid-Solid technique. Our products, the loquat-like nanostructures, hint that I could acquire nanorods of nanowires as long as I control the lateral growth appropriately. However, I still reap a lot from theses nanostructures. Firstly, they are evident to be grown by VLS process and show the single crystallinity. Secondly, I get the idea of temperature dependent growth conditions impacted more profoundly than Oxygen flow dependent cases on the crystal morphology and PL spectra. The PL measurement results showed that In_2O_3 nanoloquats could emit different broadband luminescence peaks in the range of 410~620 nm by adjusting oxygen flow rates and growth temperatures. Due to the different amount of oxygen vacancies prepared by different growth conditions, the optical transition energy of the In_2O_3 nanoloquats could become tunable, which could be conducive to applications to white light illumination.

Chapter 5   **Future work and prospect**

I regard I could start from the nanoloquat nanostructures because of their potential of forming nanorods. After appropriately controlling the lateral growth, i.e. to grow thinner and longer nanoloquats, I believe I will not lag far behind the achievement of nanorods. In addition to structural improvement, I consider the nanorods or nanowires could be worth investigating into their quantum confinement effect in the optimal size comparable with their Bohr radius. Other than fundamental structural and optical analyses undertaken as usual, I think extending the scope to electronic device is also crucial. Such the application to field effect transistors and field emission devices are in need of high-performance conductive channel and high efficiency emitter as expected.

Figures
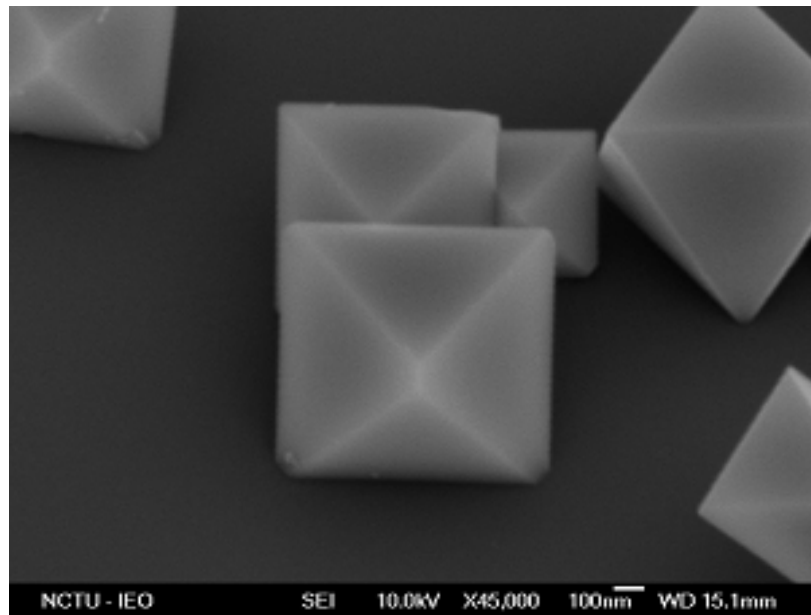
(a)
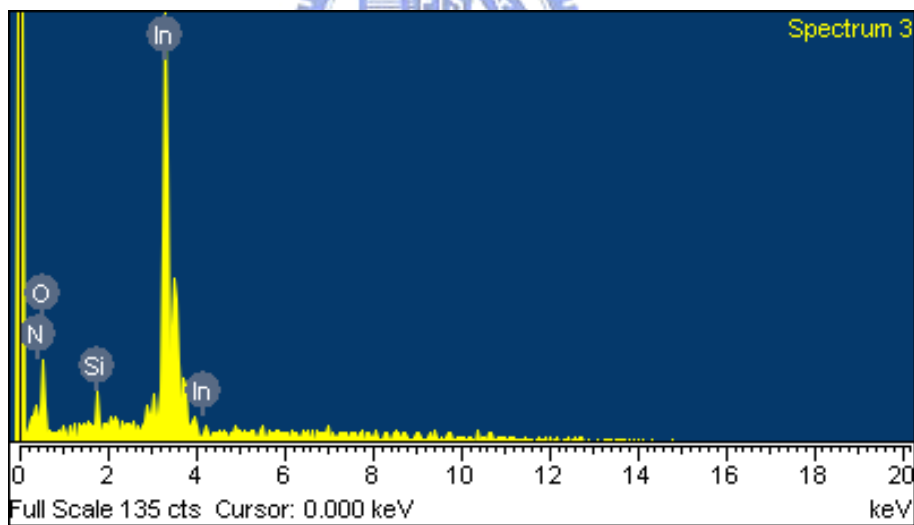
(b)

Fig. 3-1-1 (a) A typical SEM image of indium oxy-nitride nanoparticles with well-shape octahedron grown on a Si substrate. (b) EDS results of indium oxy-nitride nanoparticles.
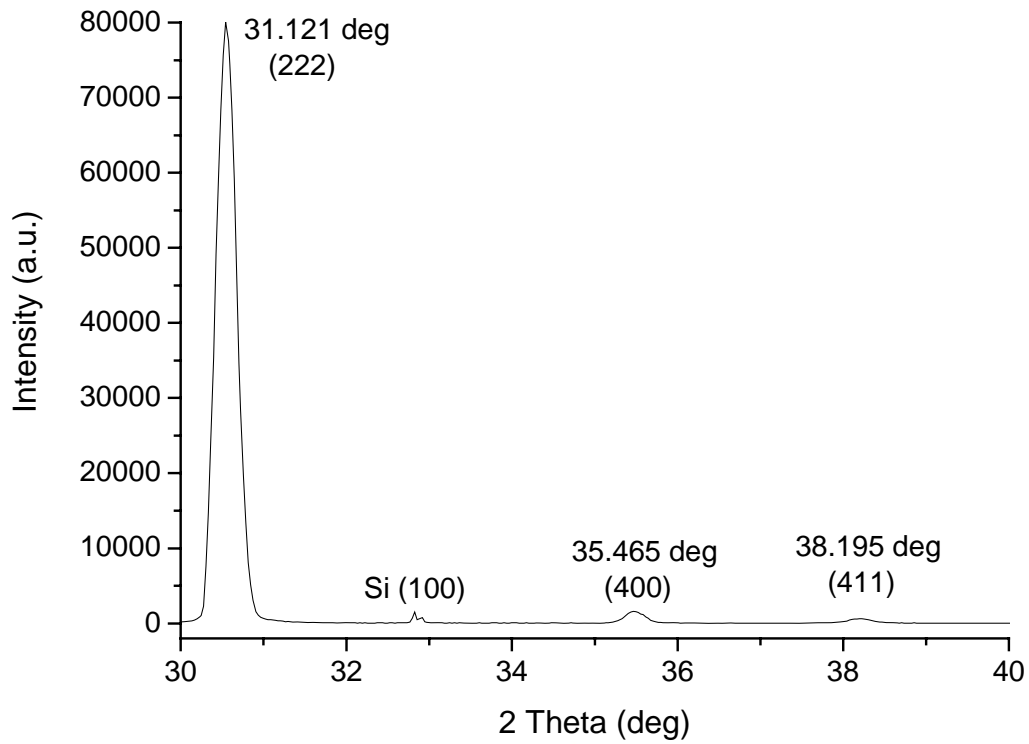
Fig. 3-1-2 XRD results of indium oxy-nitride nanoparticles on Si (100) substrate. The

numbers above the peaks correspond to the (*hkl*) values of the cubic structure.
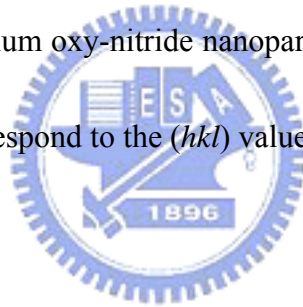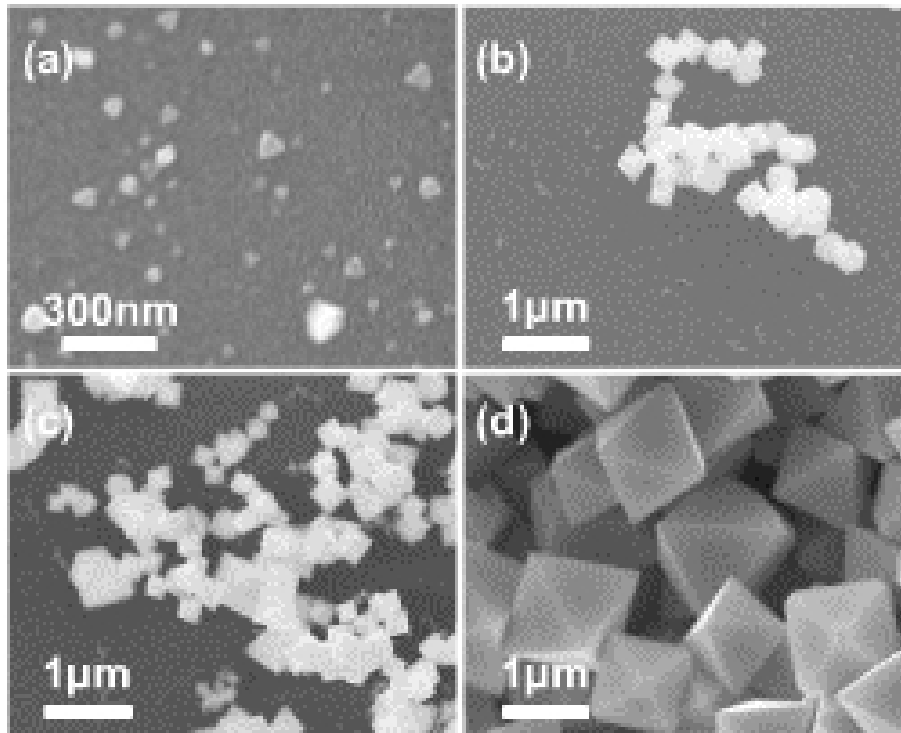
Fig. 3-1-3 SEM images of indium oxy-nitride nanoparticles grown at different

temperature. (a)-(d): 600, 700, 800, and 900 ℃.
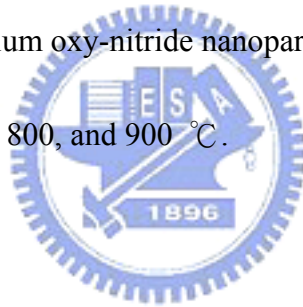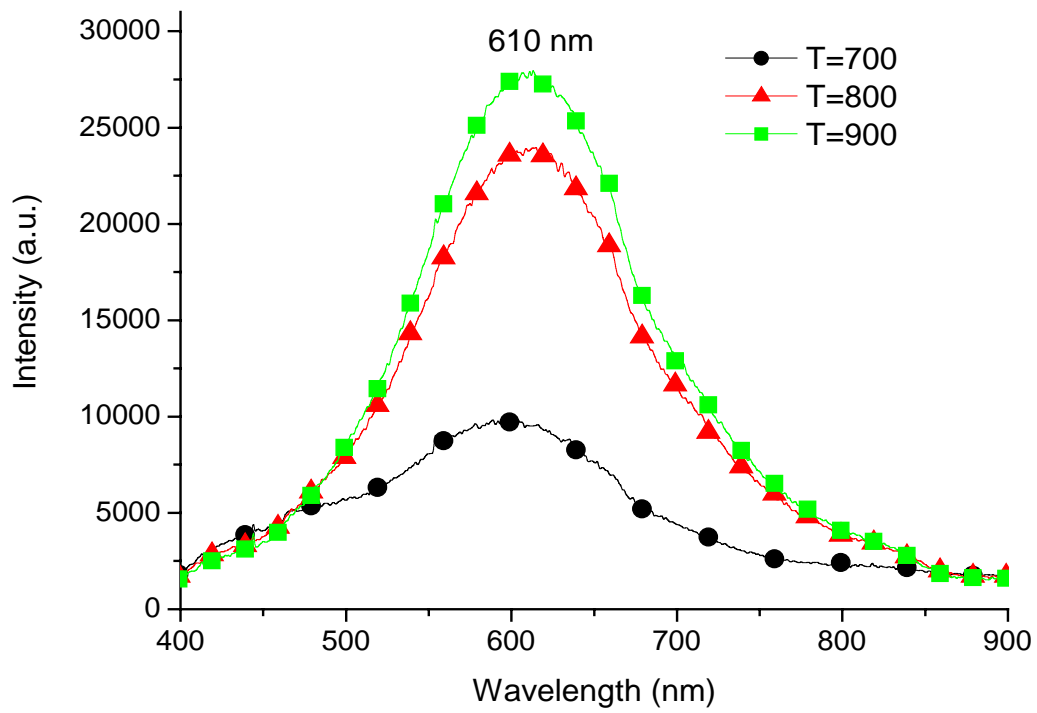
Fig. 3-1-4 PL spectra of indium oxy-nitride nanoparticles grown at different

temperatures for 30 min.
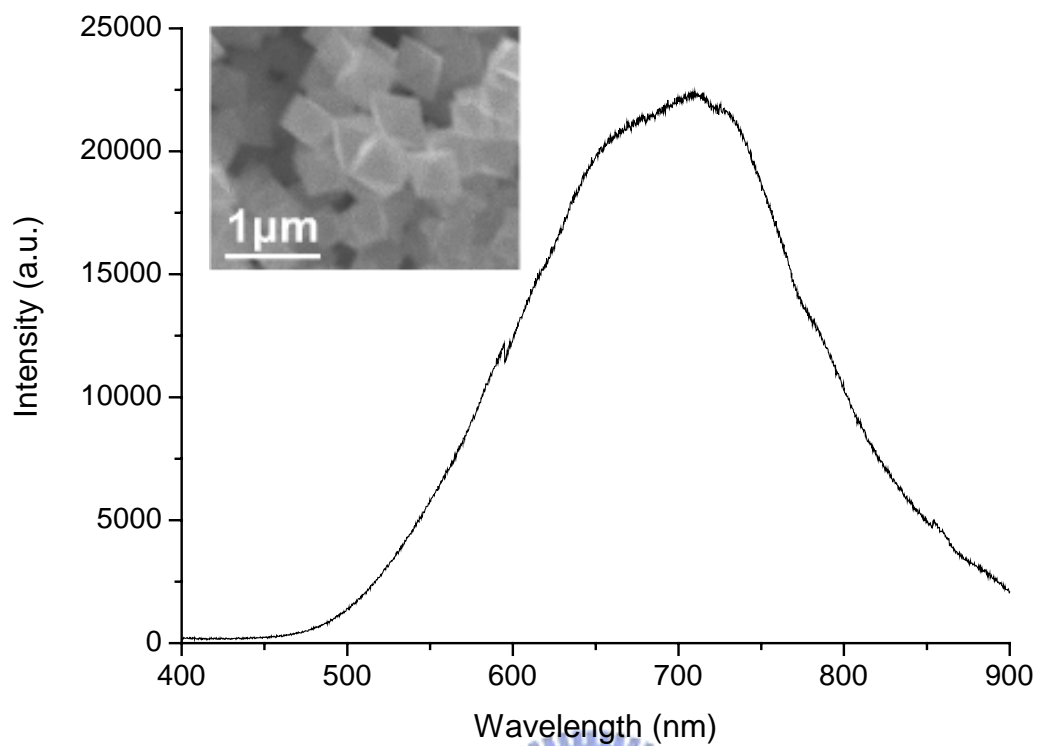
Fig. 3-1-5 PL spectrum of indium oxy-nitride nanoparticles grown at 900 ℃ for 150

min. The insert SEM image reveals the morphology of the nanoparticles.
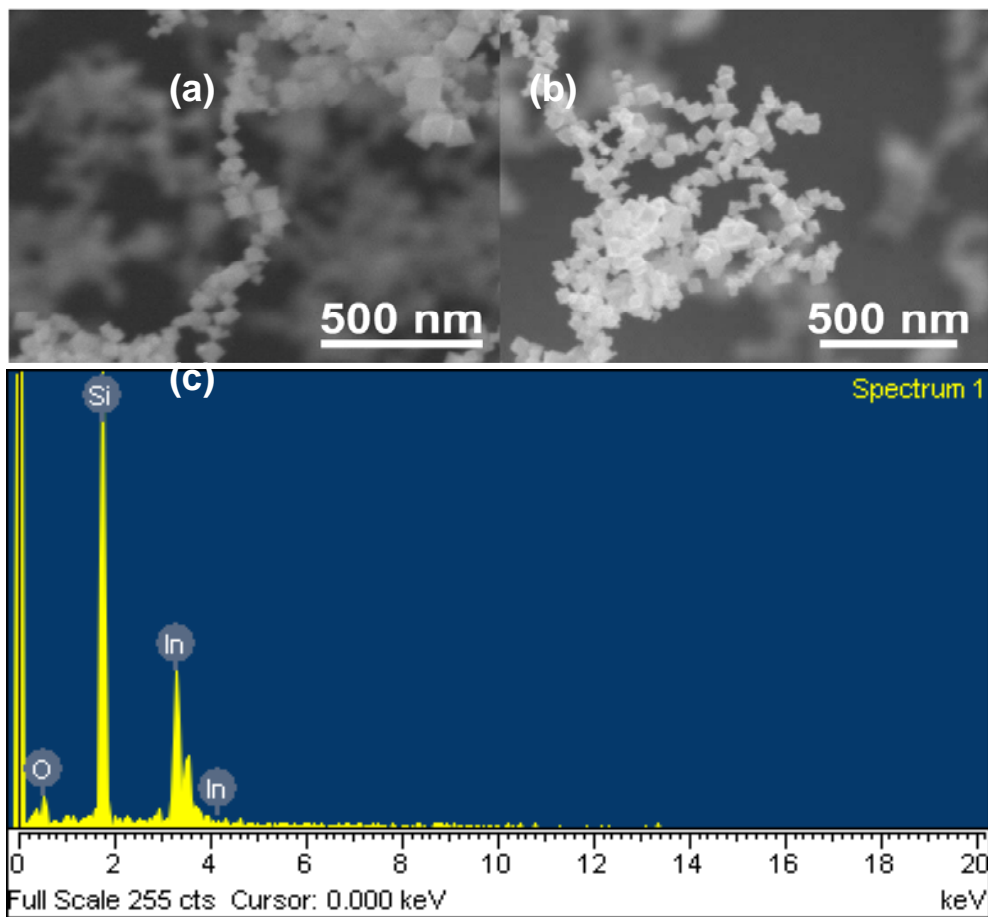
Fig. 3-2-1 (a)(b) Seclected area SEM images of In$_2$O$_3$ nanochains grown on a Si substrate. (c) EDS results of In$_2$O$_3$ nanochains.
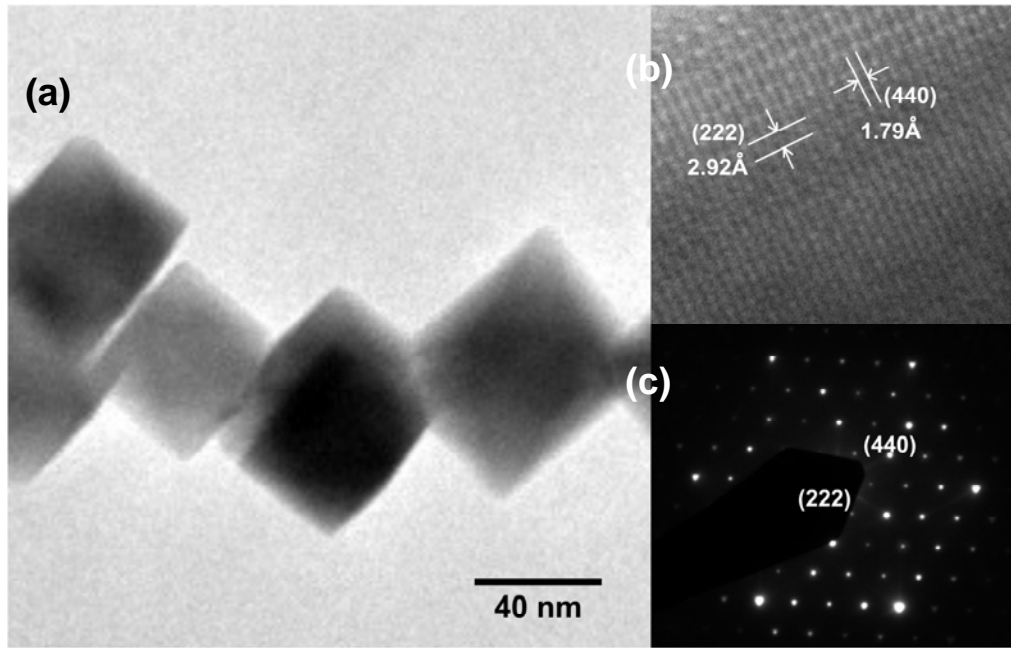
Fig. 3-2-2   (a) TEM bright-field image of part of a nanochain. (b) HRTEM image of

the nanochain. (c) The corresponding selected area electron diffraction pattern.
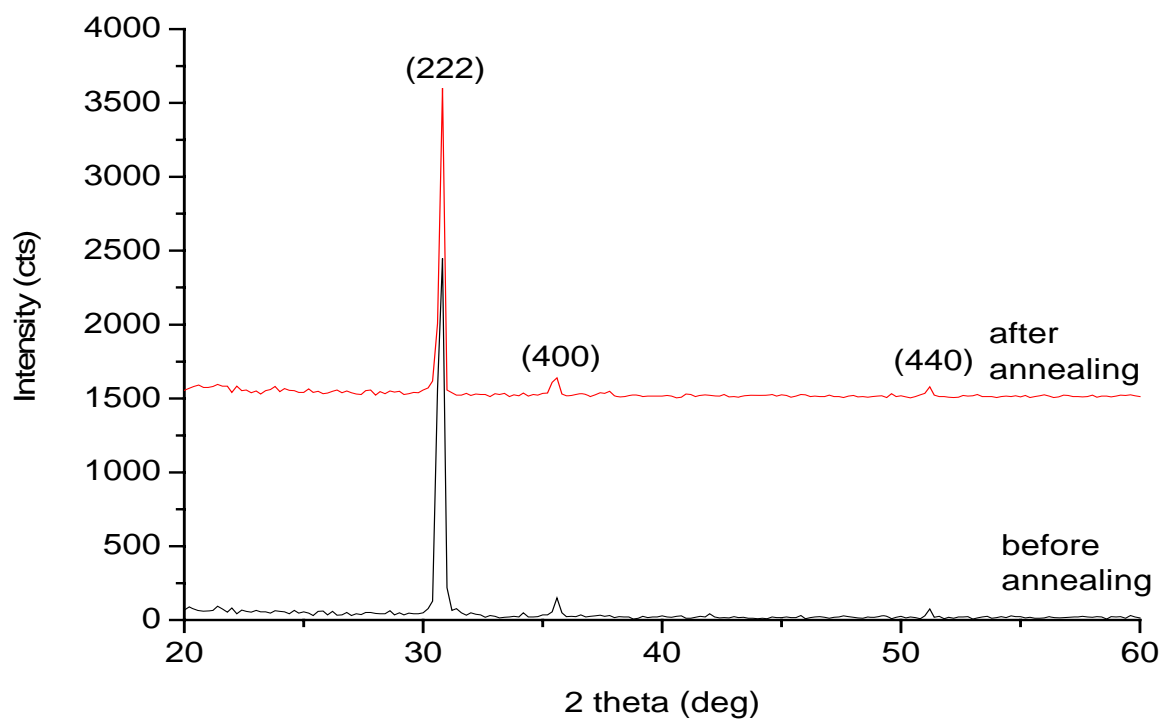
Fig. 3-2-3   XRD pattern of the In_2O_3 nanochains on Si substrate. The numbers above

the peaks correspond to (*hkl*) values of the cubic structure.
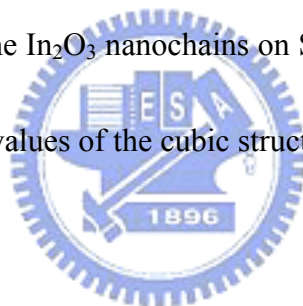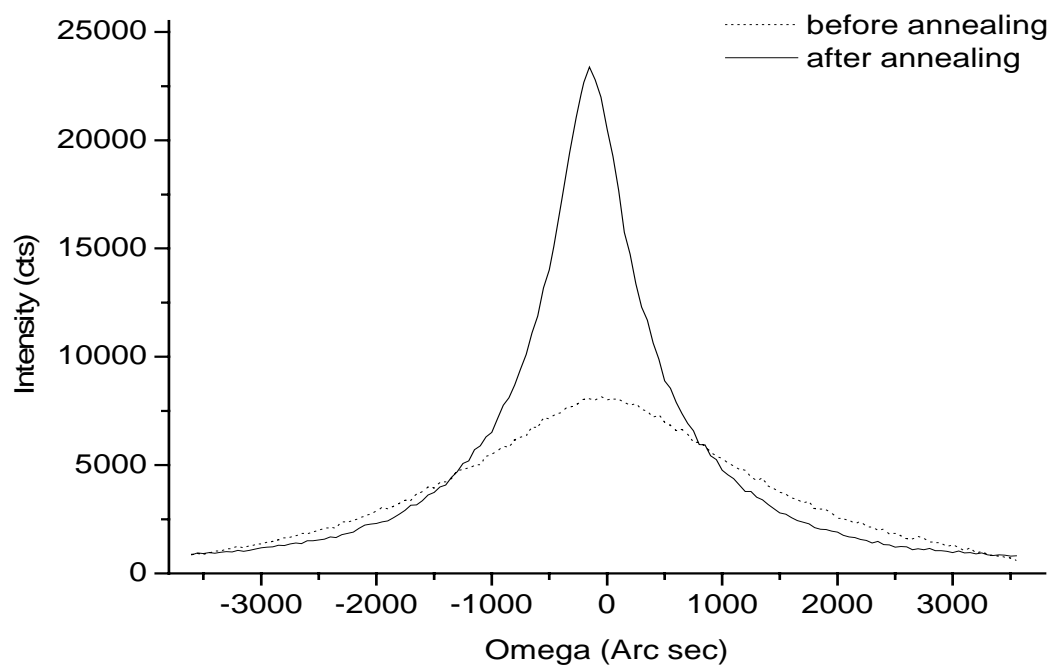
Fig. 3-2-4　XRD ω-scan data from the In$_2$O$_3$ nanochains.
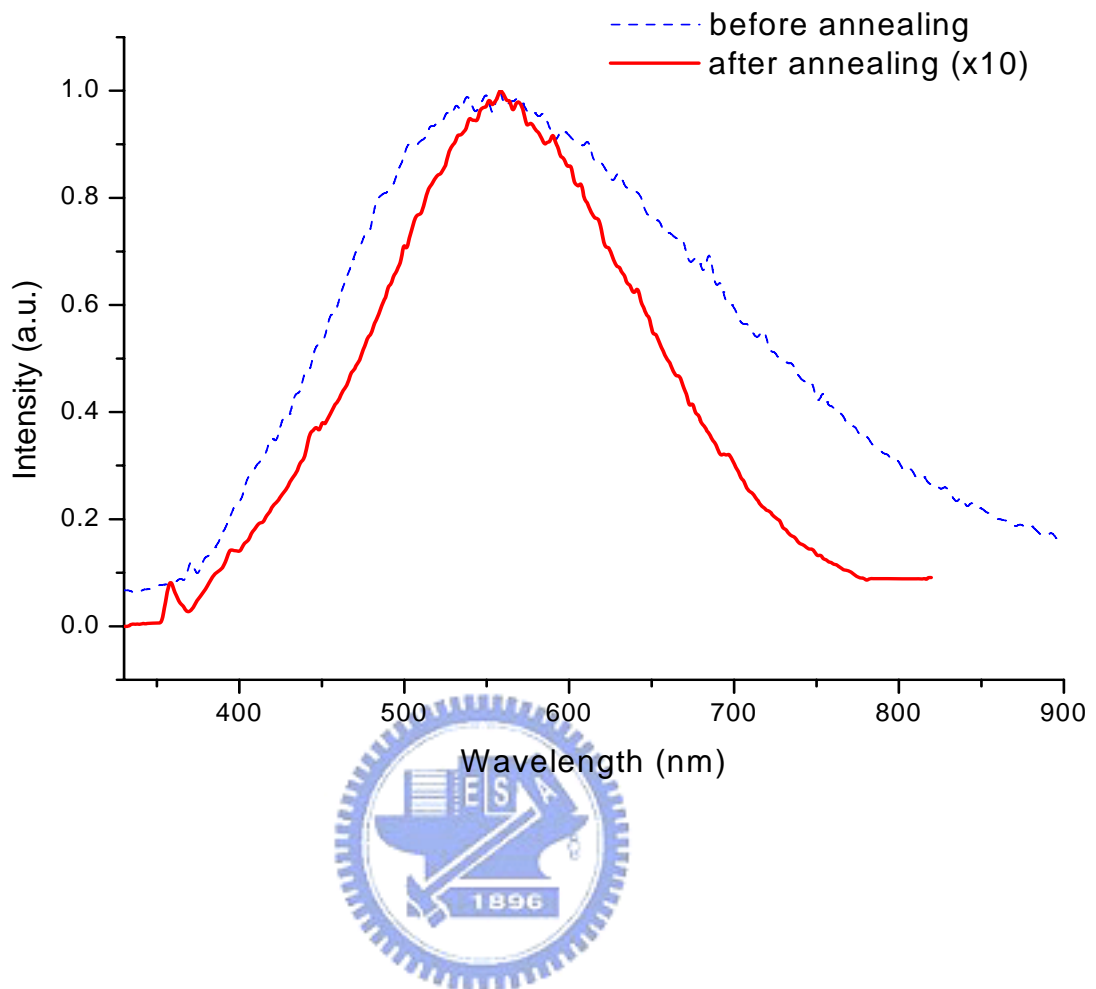
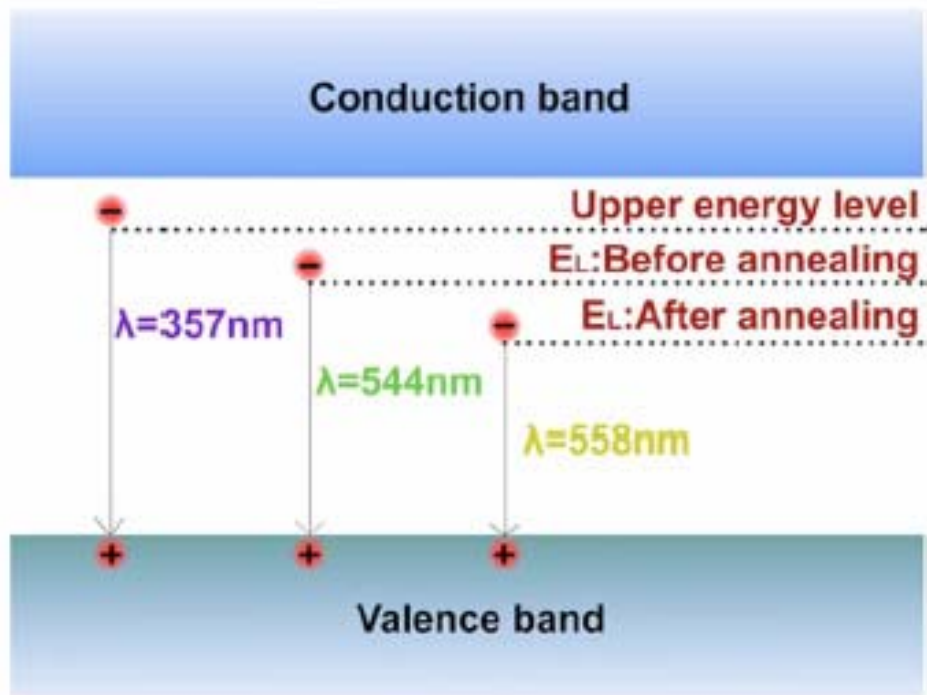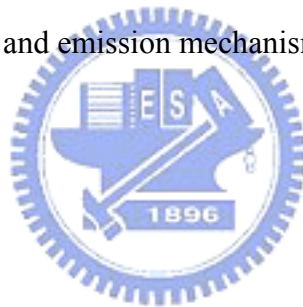Fig 3-2-5. Room temperature PL spectra of In_2O_3 nanochains with He-Cd laser excitation of 325 nm.

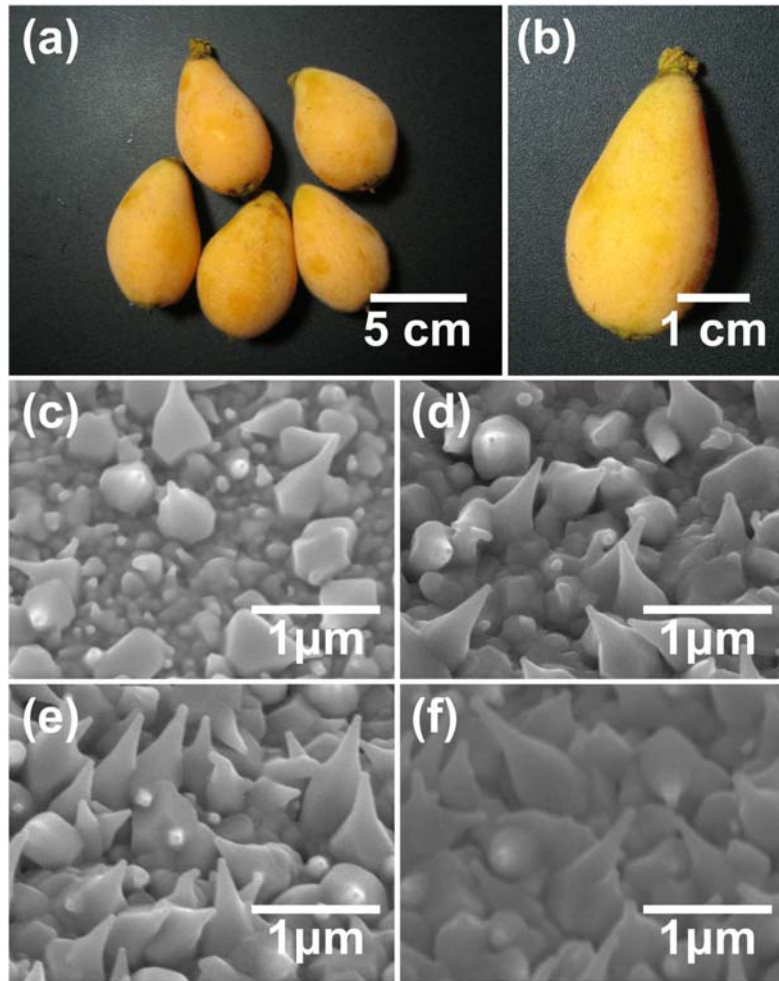Fig. 3-2-6   Transition and emission mechanisms for In_2O_3 nanochains.

Fig. 3-3-1   (a)(b) Photographs of real loquats. (c)~(f) SEM images of In_2O_3 nanoloquats grown by using different oxygen flow rates of 50, 100, 150 and 200 sccm, respectively.
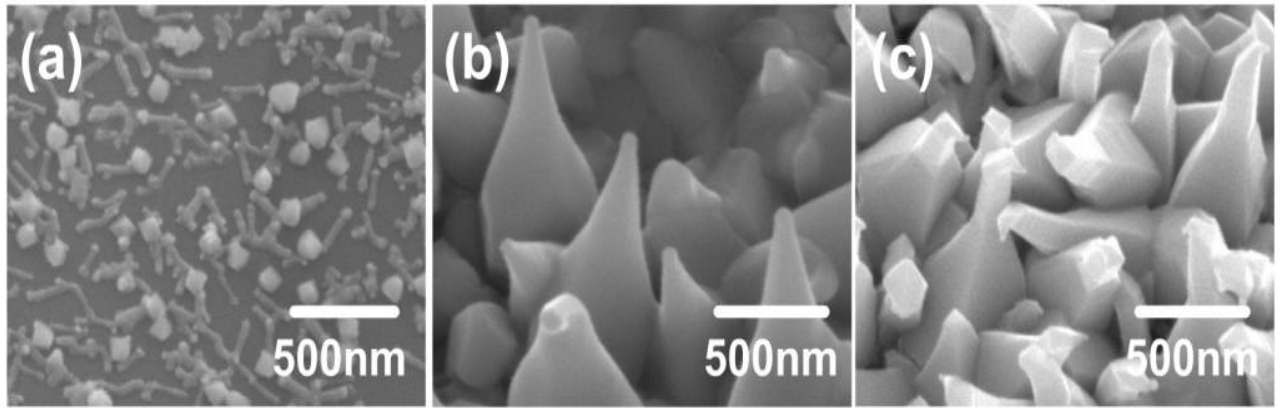
Fig. 3-3-2   (a)~(c) SEM images of In_2O_3 nanoloquats grown by using different growth temperatures of 500 ^{0}C, 700 ^{0}C, and 900 ^{0}C, respectively.
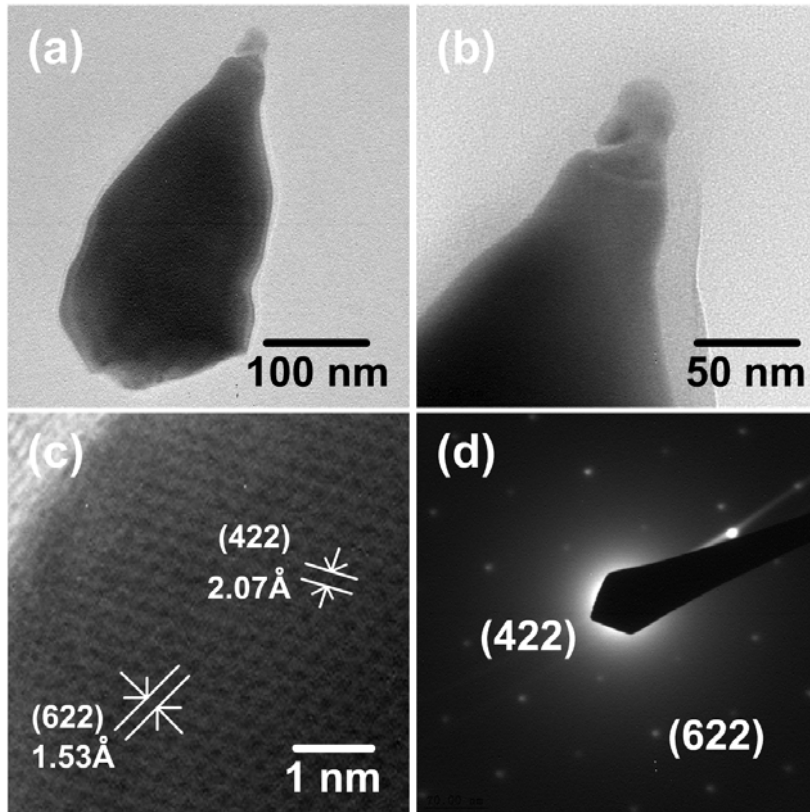
Fig. 3-3-3　(a)(b) TEM images of the In$_2$O$_3$ nanoloquats tip. (c) High-resolution

TEM images of part of the In$_2$O$_3$ nanoloquats. (d) The corresponding selected area

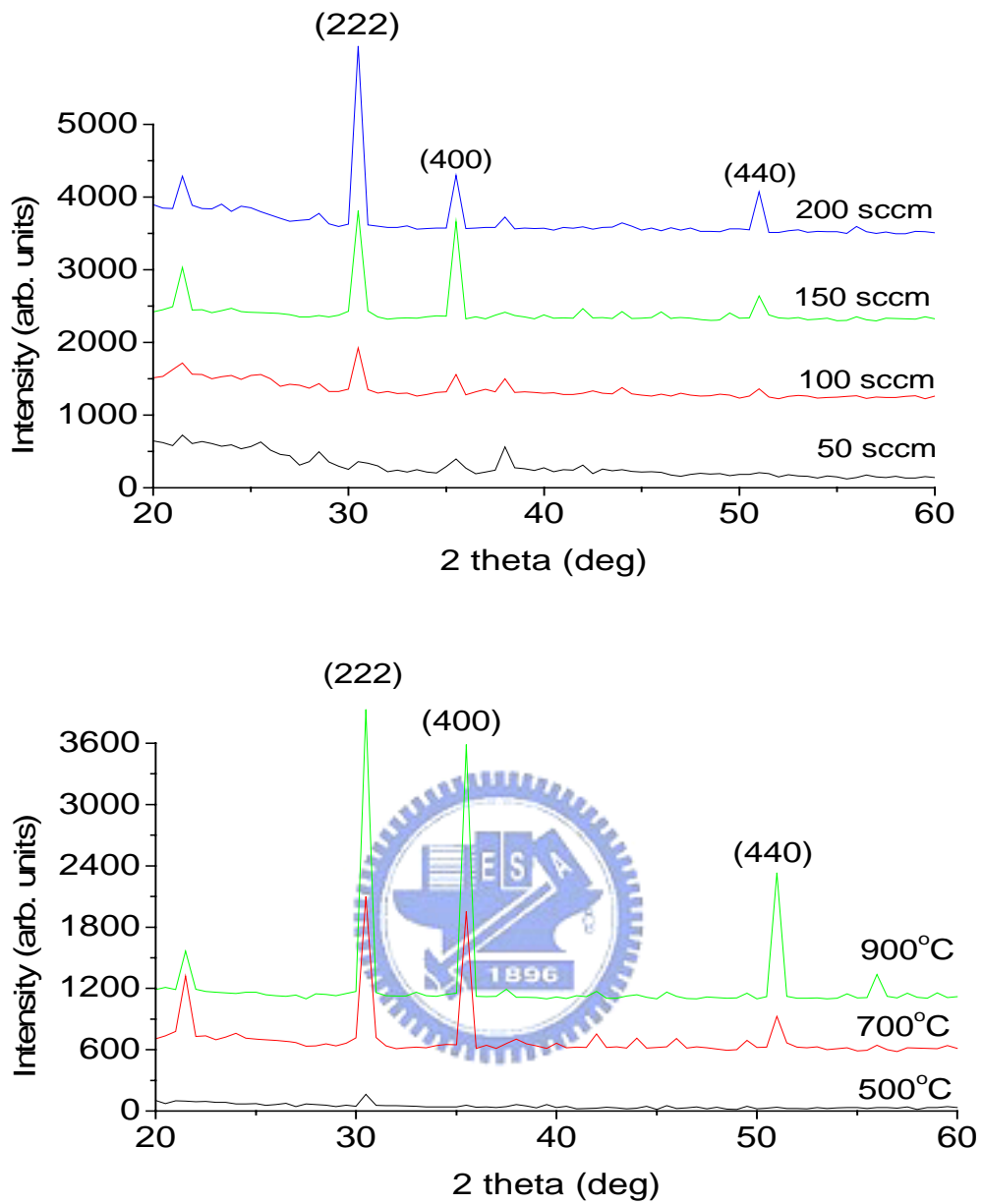electron diffraction pattern of the In$_2$O$_3$ nanoloquats.

Fig. 3-3-4   XRD pattern of the In$_2$O$_3$ nanoloquats grown in different oxygen flow

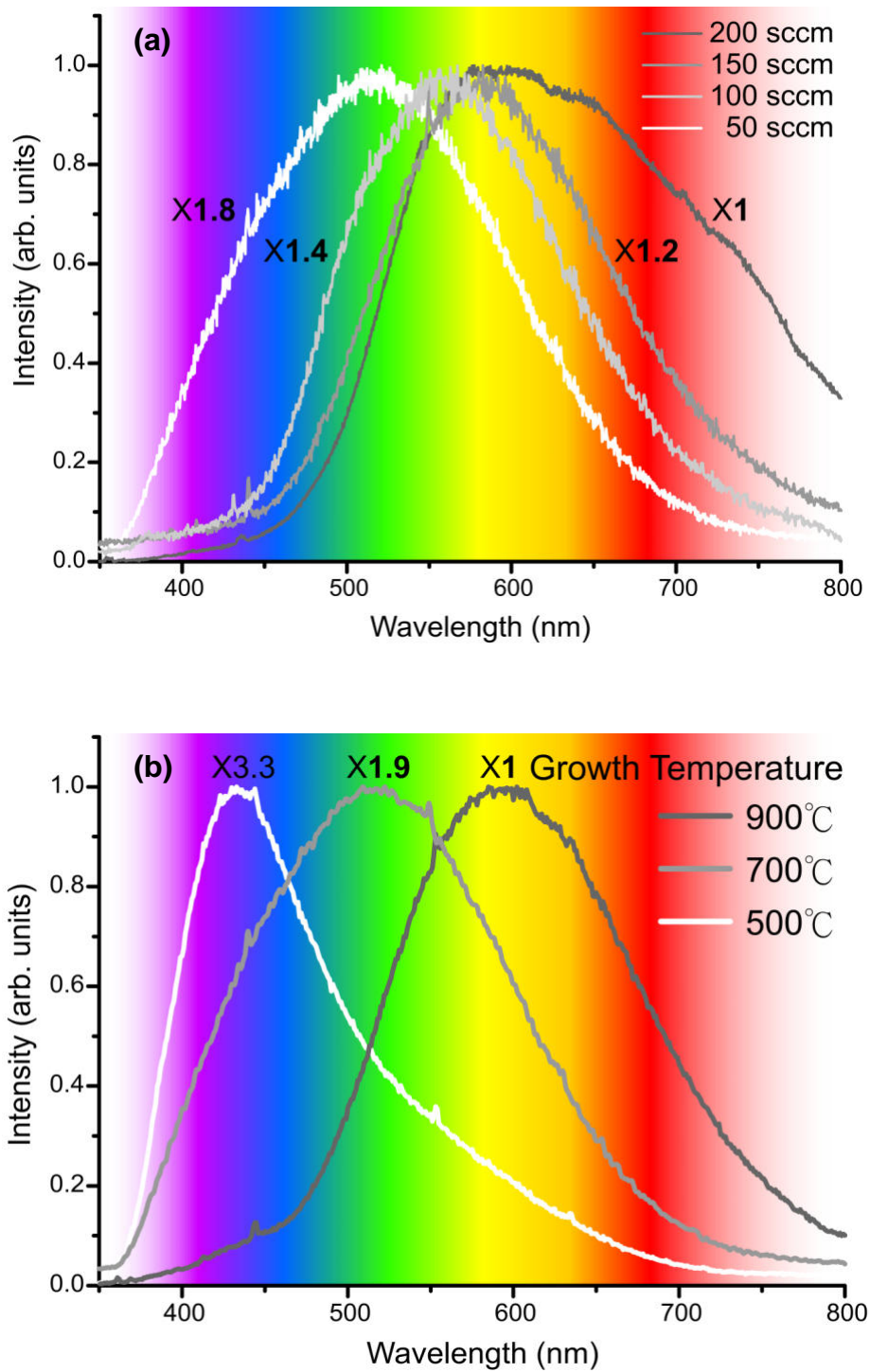rates (a) and different growth temperatures (b).

Fig. 3-3-5 Room temperature PL spectra of the In$_2$O$_3$ nanoloquats grown by using

different oxygen flow rates (a) and different growth temperatures (b).

Reference

[1] *Physics of Quantum Well Devices* (Ed: B. R. Nag), Kluwer, Dordrecht, The Netherlands (2000).

[2] *Molecular Beam Epitaxy: Fundamentals and Current Status* (Eds: M. A. Herman, H. Sitter), Springer, Berlin (1996).

[3] P. Alivisators, *Pure Appl. Chem.* **72**, 3 (2000).

[4] M. Nirmal, L. Brus, *Acc. Chem. Res.* **32**, 407 (1999).

[5] V. I. Klimov, A. A. Mikhailovsky, S. Xu, A. Malko, J. A. Hollingsworth, C. A. Leatherdale, H. J. Eisler, M. G. Bawendi, *Science* **314**, 290 (2000).

[6] D. L. Klein, R. Roth, A. K. L. Lim, A. P. Alivisators, P. L. McEuen, *Nature* **389**, 699 (1997).

[7] H. Peterson, L. Baath, N. Carlsson, W. Seifert, L. Samuelson, *Appl. Phys. Lett.* **79,** 78 (2001).

[8] A. N. Shipway, E. Katz, I. Willner, *Chem. Phys.* **1**, 18 (2000).

[9] J. Phillips, *J. Appl. Phys.* **91**, 4590 (2002).

[10] S. Coe, W. K. Woo, M. Bawendi, V. Bulovic, *Nature* **420,** 800 (2002).

[11] F. Cerrina, C. Marrian, *MRS Bull*, 56, December, (1996).

[12] Y. Xia, J. A. Rogers, K. E. Paul, G. M. Whitesides, *Chem. Rev.* **99**, 1823 (1999).

[13] "Synthesis, Electronic Properties and Applications of Indium Oxide Nanowires,"

C. Li, D. Zhang, S. Han, X. Liu, T. Tang, B. Lei, Z. Liu and C. Zhou, Annals of New York Academy of Sciences 1006, 104(2003).

[14] "Nanowires," http://www.me.berkeley.edu/nti/englander1.ppt, O. Englander, (2002).

[15] "Synthesis and photoluminescence of single-crystalline In2O3 nanowires," X. S. Peng, G. W. Meng, J. Zhang, X. F. Wang, Y. W. Wang, C. Z. Wang, L. D. Zhang, *J. Mater. Chem*. **12**, 1602 (2002).

[16] "Diameter-Controlled Growth of Single-Crystalline In2O3 Nanowires and Their Electronic Properties," C. Li, D. Zhang, S. Han, X. Liu, T. Tang, and C. Zhou, *Adv. Mater*. **15**, 143 (2003).

[17] "California State Science Fair, Project #S0524," http://www.usc.edu/CSSF/History/2004/Projects/S0524.pdf, A. Rajagopal, (2004).

[18] "Chemistry: Webelements Periodic Table," http://www.webelements.com

[19] "Periodic Table of the Elements – Indium – National Research Council Canada," http://www.nrc-cnrc.gc.ca/education/elements/el/in_e.html

[20] "Electrical and Optical Properties of Amorphous Indium Oxide," J. Bellingham, W. Phillips, C. *Adkins, J. Phys.: Condens. Matter* **2**, 6207-6221 (1990).

[21] C. Falcony, J. R.kirtley, D. J. Dimaria, T. P. Ma, T. C. Chen, *J. Appl. Phys*. **58**,

3556 (1985)

[22] C. G. Granqvist, *Appl. Phys. A:solids Surf.* **57**, 19 (1993)

[23] M. Bender, N. Katsarakis, E. Gagaoudakis, E. Hourdakis, E. Douloufakis, V. Cimalla, G. Kiriakidis, *J. Appl. Phys*. **90**, 5382 (2001)

[24] C. Li, D. H. Zhang, B. Lei, S. Han, X. L. Liu, C. W. Zhou, *J. Phys. Chem. B* **107**, 12451 (2003)

[25] X. Y. Kong, Z. L. Wang, *Solid State Commun*. **128**, 1 (2003)

[26] D. Alina Magdas, A. Cremades, J. Piqueras, *Appl. Phys. Lett*. **88**, 113107 (2006)

[27] J. Lao, J. Huang, D. Wang, Z. Ren, *Adv. Mater.* **16**, 65 (2004)

[28] C. J. Otten, O. R. Louire, M-F Yu, J. M. Cowley, M. J. Dyer, *J. Am. Chem. Soc*. **124,** 4564 (2002)

[29] X. F. Duan, C. M. Lieber, *Adv. Mater.* **12**, 298 (2000)

[30] M. S. Gudiksen, C. M. Lieber, *J. Am. Chem. Soc*. **122, 8801** (2000)

[31] Y. Zhang, H. Ago, J. Liu, M. Yumura, K. Uchida, S. Ohshima, S. Iijima, J. Zhu, X. Zhang, *J. Crys. Grow*. **264**, 363 (2004).

[32] Y. J. Zhang, N. L. Wang, S. P. Gao, R. R. He, S. Miao, J. Liu, J. Zhu, X. Zhang, *Chem. Mater*. **14**, 1654 (2002).

[33] H. J. Zhou, W. P. Cai, L. D. Zhang, *Appl. Phys. Lett*. **75**, 495 (1999).

[34] M. S. Lee, W. C. Choi, E. K. Kim, C. K. Kim, S. K. Min, *Thin Solid Films* **279**, 1
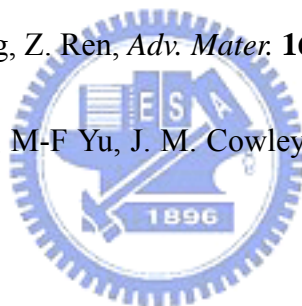
(1996).

[35]   C. X. Xu, X. W. Sun, Z. L. Dong, M. B. Yu, T. D. My, X. H. Zhang, S. J. Chua, T. J. White, *Nanotech.* **15**, 839 (2004)

[36] T. Tang, S. Han, W. Jin, X. Liu, C. Li, D. Zhang, C. Zhou, *J. Mater. Res.* **19**, 423 (2004)

[37] P. Yang, C. M. Lieber, *J. Mater. Res.* **12**, 2981 (1997)

[38] Y. C. Kong, D. P. Yu, B. Zhang, W. Fang, S. Q. Feng, *Appl. Phys. Lett.* **78**, 407 (2001)

[39] C. Liang, G. Meng, Y. Lei, F. Phillipp, L. Zhang, *Adv. Mater.* **13**, 1330 (2001)

[40] Y. Li, Y. Bando, D. Golberg, *Adv. Mater.* **15**, 581 (2003)

[41] C. Kittel, *Introduction to Solid State Physics* (Wiley, Hoboken, New Jersey 2005)

[42] http://en.wikipedia.org/wiki/Loquat

[43] M. J. Zheng, L. D. Zhang, G. H. Li, X. Y. Zhang, X. F. Wang, *Appl. Phys. Lett.* **79**, 839, (2001)

[44] C. H. Liang, L. C. Chen, J. S. Hwang, K. H. Chen, Y. T. Hung, Y. F. Chen, *Appl. Phys. Lett.* **81**, 22, (2002)

[45] H. J. Chun, Y. S. Choi, S. Y. Bae, H. C. Choi, J. Park, *Appl. Phys. Lett.* **85**, 461, (2004)

[46] K. B. Sundaram, G. K. Bhagavat, *Phys. Status Solidi* **63**, K15, (1987)

[47] H. Cao, X. Qiu, Y. Liang, Q. Zhu, M. Zhao, *Appl. Phys. Lett.* **83**, 761, (2003)